OPEN GEOMECHANICS

An open source FEM code for solving coupled thermo-poroelastoplastic processes

Matthew L. McLean [a] *& D. Nicolas Espinoza* [a]

[a] *Department of Petroleum and Geosystems Engineering The University of Texas at Austin.*

Published
5th February 2024
https://doi.org/10.5802/ogeo.17

Edited by
Jelke Dijkstra
Chalmers University of Technology,
Gothenburg, Sweden

Reviewed by
Ayman Abed,
Chalmers University of Technology
Sweden
Thomas Poulet
CSIRO Mineral Resources
Australia
Jean-Michel Pereira
Ecole des Ponts ParisTech
France

Correspondence
Matthew L. McLean
Department of Petroleum and
Geosystems Engineering
The University of Texas at Austin
Austin, TX, USA
matthewmclean@utexas.edu

Open Geomechanics is member of the Centre Mersenne for Open Scientific Publishing

Abstract. Coupled thermo-hydro-mechanical (THM) processes are ubiquitous in subsurface energy production and geological utilization and storage operations. Numerical simulation of strongly coupled THM processes is a non-trivial task, yet required to predict the performance of many applications in energy geomechanics. The majority of existing and open source THM numerical codes are not end user adaptable and do not include elastoplasticity coupled to mass and energy balance equations. This article presents an open source thermo-poroelastoplastic finite element numerical code with a fully-coupled monolithic solution strategy that is solved with Fenicsx computing platform. The formulation employs a mixed finite element scheme for pore pressure diffusivity, Petrov-Galerkin methods for energy transport, mean stress dependent yield surface, and non-associative plastic potential. The numerical solution is verified with small-scale conventional triaxial tests, including drained and undrained compression and extension. We present example simulations reaching the yield surface induced by coupled hydro-mechanical and thermal loads. In addition, we present two example large-scale applications related to geothermal energy and carbon geological storage. Results show that the numerical solution accurately predicts changes of temperature, pore pressure, and stress for a wide range of model geometries and boundary conditions, including the plastic response. The code is freely available to the general community for use and modification.

Keywords. Plasticity, Coupled processes, Numerical code, Energy geomechanics

1. Introduction

The modeling of coupled thermo-hydro-mechanical (THM) processes is of increasing importance in a range of subsurface activities including hydrocarbon recovery [Segall and Fitzgerald, 1998], geothermal energy [Evans et al., 1999, Kohl et al., 1995], nuclear waste storage [McTigue, 1986, Palciauskas and Domenico, 1982], and carbon geological storage [Jung et al., 2020, Rutqvist, 2012, Thompson et al., 2021] among others. Over the past several decades, many large-scale field tests have been conducted in these areas. A few projects in the US include: Fenton Hill enhanced geothermal system (EGS) project [Mortensen, 1978], Utah FORGE EGS project [Allis et al., 2016], Waste Isolation Pilot Plant for permanent geological storage of nuclear waste [National Research Council et al., 1996], Cranfield CO_2 geological storage project [Nemeth, 2004], and the hydraulic fracturing test site (HFTS) for multi-cluster hydraulic fracturing in shale [Ugueto et al., 2021]. Furthermore, understanding of rock shear yield and failure induced by coupled THM processes has recently gained significant interest. For example, injection of non-native fluids into the subsurface tends to reduce effective stresses, potentially creating new fractures and reactivating natural fractures and faults [Martínez-Garzón et al., 2014, Streit and Hillis, 2004]. Recent work has focused on fault reactivation in geothermal systems [Kivi et al., 2022] and in mechanical integrity of caprock response to CO_2 injection [Thompson et al., 2021], both driven by coupled changes of temperature and pore pressure.

Numerical modeling of the subsurface is important for understanding complex THM coupled responses and optimizing operating conditions [Ghassemi, 2012, Pandey et al., 2018]. However, accurate numerical simulation of THM processes including elastoplasticity poses a major challenge because (1) they can have a high degree of coupling, i.e., one process facilitates or progresses another, (2) each process operates under different spatial and time scales, (3) coupling between deformation and fluid flow becomes stronger as rock permeability decreases, and (4) all processes are sensitive to presence of rock discontinuities that reach shear yield [Phillips and Wheeler, 2008, Xia et al., 2017]. Thus, accurately predicting the porous media response requires simultaneous consideration of thermal, mechanical, and hydraulic effects. Furthermore, THM coupled feedback loops can arise in the subsurface and heighten modeling complexity. In EGS reservoirs, for example, cold injected fluid tends to flow to areas of high fracture permeability, inducing local thermal stress relaxation and increasing stress dependent permeability, causing more injection fluid to flow along the same path [McLean and Espinoza, 2023]. Hence, numerical simulation of strongly coupled fields is a non-trivial task, yet required to predict the performance of many applications in energy geomechanics.

Numerous mathematical models and computer codes have been recently developed to simulate THM processes in the subsurface including TOUGH-FLAC [Rutqvist, 2011], OpenGeoSys [Kolditz et al., 2012], FALCON (MOOSE based) [Xia et al., 2017], FEHM [Kelkar et al., 2014], CODE_BRIGHT [Olivella et al., 1996] and STOMP [Fang et al., 2013], among others (Table 1). Some of the codes are based on a well-established flow simulator with coupling of mechanically induced porosity changes through sequential solution scheme (TOUGH-FLAC, FALCON, and STOMP) while others are based on the theory of thermo-poroelasticity with monolithic solution scheme (OpenGeoSys). Preset modeling packages - both commercial and open source - limit the end user's ability to modify the underlying code, e.g., matrix assembly. Alternatively, open source computing platforms such as Fenicsx [Logg et al., 2012] allow for maximum end user control over constitutive equations, variational formulation, and solution strategy but require a high level understanding of the physics and the finite element method. Furthermore, open source software is freely available and does not present paid licensing barriers.

This paper presents the theory, verification, and application of a freely available and end user adaptable thermo-poroelastoplastic numerical solution for subsurface applications. We develop a three-dimensional THM finite element model that accounts for shear yield with the open source computing platform Fenicsx. The model implements full thermo-poroelastic coupling (some authors alternatively use tight-coupling, e.g., Lindsay et al. [2022], Wilkins et al. [2021]) and mean stress dependent yield surface. The numerical code is available at the GitHub repository listed in data availability. Section 2 describes in detail the modeling objectives, constitutive equations, elastoplastic model, and governing equations. Section 3 presents the spatial discretization and variational formulation. Section 4 verifies the numerical model against conventional drained and undrained triaxial compression/extension tests. We simulate displacement controlled and temperature controlled tests, both with and without volumetric plastic dilation. Finally, section 5 presents example simulations of (1) a closed-loop geothermal system where shear yield is thermally induced and (2) a compartmentalized reservoir subject to cold fluid injection where shear yield is driven mostly by pressure build-up.

2. Thermo-poroelastoplastic Model

2.1. Modeling Approach

The objectives of the numerical model are to: (1) incorporate stress, pressure, and porosity constitutive behavior based on the theory of thermo-poroelasticity, (2) extend traditional THM elastic coupling to include effects of rock mass inelasticity, (3) utilize a locally mass conserving finite element discretization for fluid flow, (4) preserve numerical stability in the presence of advection dominated energy transport, and (5) utilize open source computing platforms such that commercial licensing barriers are prevented. First, the evolution of porosity is important for accurate solution to THM coupled processes, which affects mass and energy transport through the connected pore space. Sequential solution schemes often utilize empirical functions or simple poroelastic models (neglecting contrasting solid matrix and pore fluid thermal expansion coefficients) to describe mechanically induced porosity changes, e.g., TOUGH-FLAC,

Table 1. Comparison between existing THM codes and our code. Discretization methods include FD: finite difference, FV: finite volume, and FE: finite element. Basis functions include CG: continuous Galerkin, DG: discontinuous Galerkin, and RT: Raviart–Thomas. We utilize a mixed form for mass balance with pressure (DG) and flux (RT) as unknowns. In our code, porosity changes arise from the theory of thermo-poroelasticity.

Code	Coupling	Plasticity	Theory of thermo-poroelasticity	Fluid flow discretization	Displacement discretization	Solution scheme	Licensing
TOUGH-FLAC	THM	Yes	No	FD	FV	seq.	commercial
OpenGeoSys	THMC	No	Yes	FE (CG)	FE (CG)	seq./mono.	open source
FALCON	THMC	Yes	No	FE (CG)	FE (CG)	seq.	open source
FEHM	THM	Yes	No	FV	FE (CG)	mono.	open source
CODE_BRIGHT	THMC	Yes	No	FE (CG)	FE (CG)	mono.	open source
COMSOL	THMC	Yes	No	FE (CG)	FE (CG)	seq./mono.	commercial
STOMP	THMC	No	No	FV	FE (CG)	seq.	commercial
Our code	THM	Yes	Yes	FE (DG/RT)	FE (CG)	mono.	open source

MOOSE, and STOMP (Table 1 - theory column). We aim to expand the storage term in the mass balance equation to reflect the theory of thermo-poroelasticity, enabling simulation of non-isothermal undrained response (e.g., cooling of a brine saturated caprock in geological carbon storage settings). Moreover, the theoretical approach requires standard poroelastic constants (Biot coefficient, drained bulk modulus, etc.) as inputs while empirical models utilize additional constants which may not be easily measured or known. Second, rock mass inelasticity is important where subsurface fluid injection or heat drainage may drive the state of stress to shear yield. Recent work in geothermal systems highlights the need of utilizing an elastoplastic constitutive law because thermal destressing can cause nonphysical states of stress in tension, well beyond the tensile strength of geothermal reservoir rocks [Im et al., 2021]. Third, high injection rates of a cool fluid in the subsurface leads to advection dominated energy transport near the injector. The standard Galerkin method tends to cause non-physical oscillations in the temperature field under this condition. Yet, accurate predictions of heat transport are important to THM coupled processes. We, therefore, aim to stabilize the energy balance equation such that no oscillations occur. Lastly, we aim for the code to provide maximum flexibility to the end user by (1) providing a reference/source code with examples (end user modifications through forking a copy of the code) and (2) utilizing open source computing platforms.

2.2. Constitutive Laws

The constitutive equations of a saturated thermo-poroelastoplastic solid are [Cheng, 2016, Wood, 2004]:

$$\mathrm{d}\sigma_{ij} = \left(K - \frac{2G}{3}\right)\delta_{ij}\mathrm{d}\varepsilon^e_{ii} + 2G\mathrm{d}\varepsilon^e_{ij} - \alpha\delta_{ij}\mathrm{d}p - \beta_d K\delta_{ij}\mathrm{d}T \quad (1)$$

$$\mathrm{d}\zeta = \alpha\mathrm{d}\varepsilon_{ii} + \frac{\mathrm{d}p}{M} - \beta_e\mathrm{d}T \quad (2)$$

$$s = \frac{c_d}{T_o} \quad (3)$$

where σ_{ij} is the Cauchy stress tensor, K is the drained bulk modulus, G is the shear modulus, ε^e_{ii} is the elastic volumetric strain, ε^e_{ij} is the elastic strain tensor, α is the Biot coefficient, p is the pore fluid pressure, β_d is the drained volumetric thermal expansion coefficient of the solid matrix ($\beta_d = \mathrm{d}\varepsilon_{ii}/\mathrm{d}T$ for a drained thermal expansion test without constraints), T is the temperature, ζ is a porosity strain equal to the variation in pore fluid content for isothermal jacketed drained loading ($\mathrm{d}p = 0$, $\mathrm{d}T = 0$), M is the Biot modulus, β_e is the volumetric thermal expansion coefficient for fluid content variation at constant bulk volume, s is entropy, and c_d is the drained specific heat at constant strain. The porosity strain ζ assumes complete saturation and defines the unit change in pore volume. Total strain $\varepsilon_{ij} = \frac{1}{2}\left[\frac{\partial u_i}{\partial x_j} + \frac{\partial u_j}{\partial x_i}\right]$ (u_i is displacement) is the summation of recoverable elastic (^{e}) and irrecoverable plastic (^{p}) parts: $\varepsilon_{ij} = \varepsilon^e_{ij} + \varepsilon^p_{ij}$. The equations above neglect heat generation at high strain rates, rapid fluid pressure changes, and assume all porosity is connected. We also neglect heat generation from high plastic strain rate (e.g., rapid and localized failure of faults) because the plastic strain rate required to significantly change the temperature is unlikely to be reached for engineering activities in the subsurface over long-times with small increments, e.g., heat extraction and fluid injection over decades. A first order approximation of the temperature change due to inelastic deformation is $\Delta T = \sigma_y \varepsilon^p / c_v$ where c_v is the volumetric heat capacity, ε^p is the inelastic shear strain, and σ_y is the shear stress where failure occurs [Ben-Zion and Sammis, 2013]. For example, consider a uniaxial (vertical) strain response to cooling for a rock with isotropic initial stress of 64 MPa (~ 5 km depth) and many preexisting fractures such that cohesion is zero. An accumulated plastic shear strain of 0.5 will only increase the rock temperature 10°C. The reader is referred to Cheng [2016] for thermo-poroelastic analytical solutions.

Altering the temperature of low permeability porous media at constant bulk volume can change the pore fluid pressure if (1) the solid matrix and pore fluid have different thermal expansion coefficients and (2) heat conduction propagates quicker than pore pressure diffusion. The magnitude

of thermally induced pressure change is controlled by [McTigue, 1986, Salimzadeh et al., 2018]:

$$\beta_e = \alpha\beta_d + n\left(\beta_f - \beta_d\right) \tag{4}$$

where n is the porosity and β_f is the volumetric thermal expansion coefficient for the saturating pore fluid. The Biot modulus is the inverse of the storage coefficient at constant bulk volume and is equal to:

$$M = \frac{K_u - K}{\alpha^2} \tag{5}$$

where $K_u = K/(1-\alpha B)$ is the undrained bulk modulus and B is Skempton's coefficient [Coussy, 2004].

To illustrate thermo-poroelastic undrained response caused by temperature changes, consider a porous medium under constant bulk volume with either low permeability or sealed boundaries such that $\zeta = 0$ (no pore fluid intake/escape). Lowering the temperature by $\mathrm{d}T$ results in a pore pressure change of $\mathrm{d}p = M\beta_e \mathrm{d}T$ and total mean stress change of $\mathrm{d}\sigma_{ii}/3 = -K_u\beta_u \mathrm{d}T$ where $\beta_u = \beta_d + nB\left(\beta_f - \beta_d\right)$ is the undrained thermal expansion coefficient. Hence, lowering the temperature induces tensile total stress changes. Mean effective stress change, however, is mitigated by pore fluid pressure decrease. For example, the difference in drained and undrained effective mean stress change is equal to $(1-\alpha)M\beta_e \mathrm{d}T$ with the drained response inducing more tensile effective stress changes.

2.3. Elastoplastic Model

First, elastic strain increments $\mathrm{d}\varepsilon^e_{ij}$ depend on change in stress and the fourth-order elastic stiffness matrix D^e_{ijkl}, $\mathrm{d}\sigma_{ij} = D^e_{ijkl}\mathrm{d}\varepsilon^e_{ij}$ [Wood, 2004]. We employ a perfectly plastic Drucker-Prager yield surface f and non-associative plastic potential g accounting for mean effective stress dependency $p' = -\frac{1}{3}\sigma'_{ii}$ to calculate plastic strain increments [Drucker and Prager, 1952]:

$$f = q - M_\phi p' - c_\phi \tag{6}$$

$$g = q - M_\psi p' \tag{7}$$

where $q = \left(\frac{3}{2}\left(\mathrm{dev}(\sigma)_{ij}\,\mathrm{dev}(\sigma)_{ij}\right)\right)^{1/2}$ is the deviatoric stress, $M_\phi = 6\sin\phi/\left(3-\sin\phi\right)$ is a parameter that matches the yield function to Mohr-Coulomb friction angle ϕ (i.e., the Drucker-Prager cone is circumscribed by the Mohr-Coulomb surface), $M_\psi = 6\sin\psi/\left(3-\sin\psi\right)$ is a non-associative parameter depending on the dilation angle ψ, and $c_\phi = 6c\cos\phi/\left(3-\sin\phi\right)$ is a parameter that matches the yield function to Mohr-Coulomb cohesive strength c. This formulation uses Terzaghi effective stress $\sigma'_{ij} = \sigma_{ij} + p\delta_{ij}$ to evaluate the yield criterion (refer to [Gueguen and Bouteca, 1999] for discussion on Biot and Terzaghi effective stress at yield). The Drucker-Prager failure criterion is chosen for ease of numerical implementation as it has a smooth yield surface, avoiding discontinuous derivatives of the yield function. Future versions of the code, however, are planned to include other failure criterion for rocks, e.g., Mohr-Coulomb, Mogi, Lade, etc.

For loading/unloading beyond the elastic regime, plastic strain increments $\mathrm{d}\varepsilon^p_{ij}$ must return the state of stress to the yield surface so that the plastic consistency conditions are satisfied: $\mathrm{d}\lambda \geqslant 0$; $f = 0$; $\frac{\partial f}{\partial \sigma'_{ij}}\mathrm{d}\sigma'_{ij} = 0$. Plastic strain increments are given by:

$$\mathrm{d}\varepsilon^p_{ij} = \mathrm{d}\lambda\frac{\partial g}{\partial \sigma'_{ij}} \tag{8}$$

where $\mathrm{d}\lambda$ is a scalar plastic multiplier. The consistency conditions and absence of strain hardening/softening permit obtaining a closed-form solution to the plastic multiplier:

$$\mathrm{d}\lambda = \frac{\frac{\partial f}{\partial \sigma'_{ij}} D^e_{ijkl}\mathrm{d}\varepsilon_{ij}}{\frac{\partial f}{\partial \sigma'_{ij}} D^e_{ijkl}\frac{\partial g}{\partial \sigma'_{ij}}} \tag{9}$$

Notice that Eq. 8 and 9 are valid for several constitutive laws, e.g., poroelastic, thermoelastic, etc. The numerator of Eq. 9 computes the stress increment induced by the total strain increment, i.e., it is equal to the stress increment without plastic response. Some plasticity formulations refer to this as the elastic trial stress increment: $\mathrm{d}\sigma'^{,e}_{ij}$ [Itasca Consulting Group, Inc., 2019]. We employ the following form of the plastic multiplier for monolithic numerical implementation:

$$\mathrm{d}\lambda = \frac{\langle f\left(\sigma'^{,e}_{ij}\right)\rangle_+}{f'\left(D^e_{ijkl}\frac{\partial g}{\partial \sigma'_{ij}}\right)} \tag{10}$$

where $\sigma'^{,e}_{ij} = \sigma'_{ij}\left(\mathrm{d}\varepsilon_{ij} + \varepsilon^{e,k-1}_{ij}, p^k, T^k\right)$ is the elastic trial stress evaluated with current total strain increment and elastic strain from the previous time step $(k-1)$, $\langle f\rangle_+ = 1/2\left(f + |f|\right)$ is the positive part of the yield function, and f' is the yield function without the cohesion constant, i.e., $f' = f + c_\phi$. This form returns $\mathrm{d}\lambda > 0$ if the yield function - assuming no plastic response - becomes larger than zero and returns $\mathrm{d}\lambda = 0$ if the state of stress remains in the elastic region. Note that the elastic trial stress reduces to $\sigma'^{,e}_{ij} = \sigma'_{ij}\left(\varepsilon^k_{ij} - \varepsilon^{p,k-1}_{ij}, p^k, T^k\right)$ after expanding the strains. Moreover, the denominator of Eq. 10 is a constant in absence of strain hardening/softening, and it is equal to: $f'\left(D^e_{ijkl}\frac{\partial g}{\partial \sigma'_{ij}}\right) = 3G + KM_\phi M_\psi$. An exponential strain softening model is formulated and verified in Appendix A.

Lastly, the elastoplastic tangent stiffness matrix D^{ep}_{ijkl} describes modulus reduction at yield, and it is equal to:

$$D^{ep}_{ijkl} = D^e_{ijkl} - \frac{D^e_{ijkl}\frac{\partial g}{\partial \sigma'_{ij}}\frac{\partial f}{\partial \sigma'_{ij}}D^e_{ijkl}}{3G + KM_\phi M_\psi} \tag{11}$$

For perfectly plastic materials, the elastic moduli degrade from initially large values (K, G) to zero, i.e., total strain changes cause no change of stress.

2.4. Governing Equations

Fluid flow and heat transfer in a deformable porous solid are coupled. Changes of solid strain, pore pressure, and/or temperature result in changes of momentum, mass, and energy balance [Bai and Abousleiman, 1997]. The quasi-static equations of a fluid saturated and non-isothermal porous

system are [Biot, 1941, Palciauskas and Domenico, 1982]:

Solid equilibrium:

$$\frac{\partial}{\partial x_i}\left(D^{ep}_{ijkl}\left(\frac{\partial u_k}{\partial x_l}-\frac{\beta_d}{3}\delta_{kl}\Delta T\right)\right)-\alpha\frac{\partial p}{\partial x_i}=b_i \tag{12}$$

Mass balance:

$$\frac{\alpha^2}{K_u-K}\frac{\partial p}{\partial t}-\frac{k}{\mu}\frac{\partial^2 p}{\partial x_i^2}+\alpha\frac{\partial \varepsilon_{ii}}{\partial t}-\beta_e\frac{\partial T}{\partial t}=f^p \tag{13}$$

Energy balance:

$$\frac{\partial T}{\partial t}-\alpha_T\frac{\partial^2 T}{\partial x_i^2}+\frac{(\rho c)_f}{(\rho c)_s}q_i^f\frac{\partial T}{\partial x_i}=f^T \tag{14}$$

where b_i is the gravitational body force, k is the permeability, μ is the pore fluid viscosity, f^p is fluid source/sink, α_T is the solid matrix thermal diffusivity, ρc is the volumetric heat capacity of the solid matrix (s) and fluid (f) phases, q_i^f is the Darcy velocity, and f^T is heat source/sink. The mass balance equation assumes permeability and pore fluid viscosity are constants and, thus, they are taken out of the divergence operator. Thermal strain ($\frac{\beta_d}{3}\delta_{kl}\Delta T$) is calculated with respect to the in-situ temperature distribution.

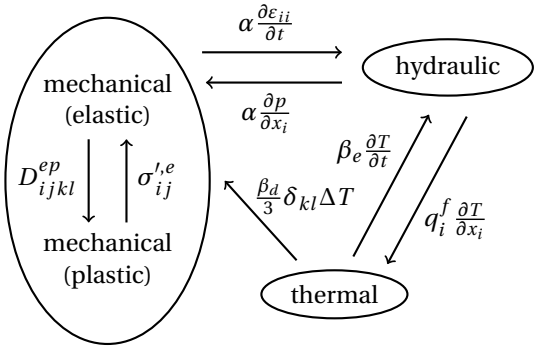

Figure 1. Thermo-poroelastoplastic coupling scheme considered in this work.

In addition to traditional THM elastic coupling, this work considers the influence of yield on solid equilibrium and coupling scheme (Figure 1). The added coupling of elastoplasticity consists of evaluating the yield criterion and returning either (1) zero plastic strain if the state of stress is in the elastic region or (2) non-zero plastic strain increment if thermal, hydraulic, and mechanical loads drive the state of stress to shear failure. A brief description of the considered couplings is:

- $\alpha\frac{\partial \varepsilon_{ii}}{\partial t}$: fluid intake and escape caused by bulk volume changes
- $\alpha\frac{\partial p}{\partial x_i}$: alteration of total stress caused by pore fluid pressure
- $\frac{\beta_d}{3}\delta_{kl}\Delta T$: influence of thermal expansion and contraction on total strain
- $\beta_e\frac{\partial T}{\partial t}$: fluid intake and escape caused by contrasting thermal expansion between solid matrix and pore fluid
- $q_i^f\frac{\partial T}{\partial x_i}$: convective energy transport by fluid flow through connected pore space
- D^{ep}_{ijkl}: evaluation of elastoplastic tangent stiffness matrix (moduli degradation at yield)
- $\sigma'^{,e}_{ij}$: plastic correction to return the state of stress to the yield surface

3. Numerical Solution

The governing equations are derived in the weak form and solved with the freely available Fenicsx computing platform [Logg and Wells, 2010], relying on the nonlinear solver provided in dolfiny [Habera and Zilian, 2022]. This approach is ideal to tailor the code to solve subsurface problems, a function that is rarely available in commercial codes and preset open source codes, e.g., full THM coupling and poroelastoplasticity. The numerical solution was verified to work with Fenicsx version 0.6.0. Additional changes may be required for future releases.

Coupled fluid flow and geomechanics is often solved with a displacement-pressure formulation. However, conditional stability arises with continuous finite elements in the presence of undrained response where small time steps may cause oscillations [Kim, 2010]. We, therefore, utilize continuous elements for displacements and a mixed space for fluid flow consisting of piecewise constant for pressure and Raviart-Thomas elements for Darcy velocity. The main advantages of this formulation are: (1) it provides local mass conservation, (2) it avoids pressure oscillations - if storage coefficient is not zero, (3) it eliminates post-processing techniques required to recover the velocity field, and (4) it provides greater accuracy in the velocity field which may be of high interest for coupling with advective heat transport [Berger et al., 2017, Phillips and Wheeler, 2007a]. The main disadvantage, however, is that the mixed method increases total degrees of freedom. We balance this through utilizing lowest-order elements for pressure and velocity. Furthermore, oscillations tend to occur when thermal advection dominates energy transport and utilizing continuous Galerkin methods. We, therefore, use the Petrov-Galerkin method for the temperature field to avoid numerical oscillations [Brooks and Hughes, 1982].

This formulation solves for solid displacement u_i, plastic strain ε^p_{ij}, fluid pressure p, Darcy velocity q_i^f, and temperature T that is in local equilibrium between rock matrix and pore fluid. Suitable test function spaces for thermo-poroelastoplasticity are:

$$\begin{aligned}
V_u &= \left\{\delta u_i \in H^1(\Omega)\,|\,\delta u_i = u_D \qquad \text{on } \partial\Omega\right\}\\
V_\varepsilon &= \left\{\delta\varepsilon^p_{ij} \in L^2(\Omega)\right\}\\
V_p &= \left\{\delta p \in L^2(\Omega)\right\}\\
V_q &= \left\{\delta q_i^f \in H(\mathrm{div})\,|\,\delta q_i^f n_i = q_D \qquad \text{on } \partial\Omega\right\}\\
V_T &= \left\{\delta T \in H^1(\Omega)\,|\,\delta T = T_D \qquad \text{on } \partial\Omega\right\}
\end{aligned} \tag{15}$$

where Ω is the three-dimensional domain, $\partial\Omega$ is the domain boundary, "δx" is the test function, and the subscript ($_D$) is the Dirichlet boundary condition [Brezzi et al., 1985, Haagenson et al., 2020, Logg et al., 2012]. Constant pore pressure boundary conditions are enforced weakly

through the variational formulation. $H^1(\Omega)$, $L^2(\Omega)$, and $H(\text{div})$ are the Sobolev spaces [Logg et al., 2012]. Time integration is performed with the implicit Euler method: $\frac{\partial(\cdot)}{\partial t} = \left[(\cdot)^t - (\cdot)^{t-\Delta t}\right]/\Delta t$. The Euler method is used for simplicity in deriving the variational form. Recent work shows that the implicit Euler scheme exhibits similar convergence profiles to that of higher order schemes for the displacement-mixed discretization of poroelasticity [Phillips and Wheeler, 2007b].

The solution scheme is monolithic, solving all dependent variables simultaneously. Therefore, Newton iteration and a direct linear solver are employed to solve the coupled nonlinear equations through PETSc [Balay et al., 2022]. Although requiring more computation time, the direct linear solver is chosen for ease of implementation over more advanced Newton-Krylov methods for poroelasticity [Franceschini et al., 2021, Frigo et al., 2021]. The solution strategy is shown in Algorithm 1 (note: J is the Jacobian, F is the total residual, x is the solution vector, i is the iteration number, and k is the current time step).

Algorithm 1 Monolithic solution scheme

set $t = 0$, $k = 0$
set initial values $\left(\cdot^{k-1}\right)$
while $t \leqslant t_{\max}$ **do**
  while error $\leqslant$ tolerance **do**
    linear solve $J(x_i)\,\Delta x_i = -F(x_i)$
    update $x_{i+1} = x_i + \Delta x_i$
    $i \mathrel{+}= 1$
  if $\frac{1}{\text{volume}}\int_\Omega f\left(\sigma'_{ij}\right)\mathrm{d}\Omega \geqslant$ tolerance **then**
    repeat step 4
  set $x^{k-1} = x^k$
  $t \mathrel{+}= \Delta t$
  $k \mathrel{+}= 1$

Multiplying the governing equations by a test function and integrating over the domain, results in the discrete variational thermo-poroelastoplastic problem: find $u_i^k \in V_u$, $\varepsilon_{ij}^{p,k} \in V_\varepsilon$, $p^k \in V_p$, $q_i^{f,k} \in V_q$, and $T^k \in V_T$ such that

Solid equilibrium:

$$\int_\Omega \left(\sigma_{ij}^k \delta\varepsilon_{ij} - b_i \delta u_i\right)\mathrm{d}\Omega = \int_{\partial\Omega} (t_i \delta u_i)\,\mathrm{d}\partial\Omega \tag{16}$$

Plastic strain:

$$\int_\Omega \left(\left(\varepsilon_{ij}^{p,k} - \varepsilon_{ij}^{p,k-1}\right) - \mathrm{d}\lambda \frac{\partial g}{\partial \sigma'_{ij}}\right)\delta\varepsilon_{ij}^p \mathrm{d}\Omega = 0 \tag{17}$$

Mass balance:

$$\int_\Omega \left(\alpha\left(\varepsilon^k - \varepsilon^{k-1}\right) + \frac{1}{M}\left(p^k - p^{k-1}\right) + \Delta t \frac{\partial q_i^{f,k}}{\partial x_i}\right. \tag{18}$$
$$\left. -\beta_e\left(T^k - T^{k-1}\right)\right)\delta p \mathrm{d}\Omega = \int_\Omega \Delta t f^p \delta p \mathrm{d}\Omega$$

Fluid flux:

$$\int_\Omega \left(\frac{\mu}{k} q_i^{f,k} \delta q_i^f - p^k \frac{\partial \delta q_i^f}{\partial x_i}\right)\mathrm{d}\Omega = \tag{19}$$
$$-\int_{\partial\Omega} p_D \left(n_i \delta q_i^f\right)\mathrm{d}\partial\Omega$$

Energy balance:

$$\int_\Omega \left(\frac{1}{\Delta t}\left(T^k - T^{k-1}\right)\delta T + \alpha_T \frac{\partial T^k}{\partial x_i}\frac{\partial \delta T}{\partial x_i}\right)\mathrm{d}\Omega \tag{20}$$
$$+\int_\Omega \left(\frac{(\rho c)_f}{(\rho c)_s} q_i^{f,k} \frac{\partial T^k}{\partial x_i}\delta T\right)\mathrm{d}\Omega$$
$$= \int_\Omega \left(f^T \delta T - \frac{h}{2|q_i^{f,k}|} q_i^{f,k} \frac{\partial \delta T^k}{\partial x_i} R\right)\mathrm{d}\Omega$$

where $\left(\cdot^k\right)$ is the solution at time t, $\left(\cdot^{k-1}\right)$ is the solution at time $t - \Delta t$, b_i is the gravitational body force, $t_i = \sigma_{ij} n_i$ is the applied traction (e.g., total vertical stress at the depth of the model if not using a mechanical earth model), f^p is a fluid source/sink applied as the Dirac delta function to restrict injector/producer flow rates to interior "well" nodes, p_D is the Dirichlet pressure boundary condition imposed weakly, f^T is a heat source/sink for injector wells if injection fluid is at a different temperature than the reservoir, h is the equivalent mesh element diameter, and R is the residual of the strong form energy balance equation (Eq. 14). The variational form of the energy balance equation is stabilized with the streamline upwind Petrov-Galerkin method [Brooks and Hughes, 1982]. In the mixed form for fluid flow, Dirichlet pressure boundary conditions are weakly imposed as natural conditions in Eq. 19 while Neumann boundary conditions (flux) are essential. This is opposite to the pressure only formulation where Dirichlet boundary conditions are essential and Neumann boundary conditions are natural [Pan and Rui, 2012].

4. Verification: Triaxial Simulation

We verified the numerical solution against expected theoretical solutions for conventional triaxial compression and extension tests. In this section, we consider (1) an axial displacement controlled drained compression test, (2) an axial displacement controlled undrained compression test, and (3) temperature controlled drained/undrained compression and extension tests. Undrained conditions are simulated by decreasing the permeability rather than by increasing the load rate. The modeling domain is a three-dimensional cylinder with diameter equal to 25 mm, height equal to 62.5 mm, discretized in ~ 1,390 tetrahedral elements. Total degrees of freedom are 45,799. We performed a convergence study with respect to mesh size with results available in the following sub-section. All simulations begin with an initially unloaded sample, followed by isotropic loading to a prescribed mean effective stress of 10 MPa, and driven to yield by increasing deviatoric stress. Mechanical and thermal loads are applied incrementally through a constant load rate with two modalities:

- Displacement controlled test: imposed axial strain is equal to a load rate of 0.1% per minute times the current time. Maximum axial strain is 1.5% for a total simulation time of 15 minutes.
- Temperature controlled test: imposed temperature change is equal to a thermal load rate of 16.67 °C

per minute times the current time. Maximum temperature change is 250 °C, enough to drive the state of stress to shear failure in either compression or extension under axially constrained condition. Total simulation time is also 15 minutes.

Material properties are shown in Table 2. Simulation of undrained response under constant load rate requires characteristic pore pressure diffusion time ($t_{ch} = h^2\mu/kM$ with h as the rock sample height) to be significantly larger than the time-step of 36 seconds. Hence, $t_{ch} \approx 0.004$ seconds for the drained simulations and $t_{ch} \approx 40000$ seconds for the undrained simulations. Subsections 4.2 and 4.3 present results for the three cases. The numerical solution follows conventional elasticity sign convention. Results are converted to geomechanics sign convention, e.g., compressive stress and contraction strain are positive in a post-processing step.

Table 2. Poro-elastoplastic properties for model verification.

Property	Value	Unit
Bulk modulus: K	3.5	GPa
Shear modulus: G	2.0	GPa
Biot modulus: M	8.9	GPa
Biot coefficient: α	0.9	-
Uniaxial comp. strength: UCS	5.0	MPa
Friction angle: ϕ	30	°
Dilation angle: ψ	0, 7.5	°
Permeability: k	10^{-13}, 10^{-20}	m^2
Porosity: n	0.2	-
Porous solid expansion: β_d	6×10^{-5}	1/°C
Fluid mass expansion: β_e	8×10^{-5}	1/°C

4.1. Mesh Convergence Study

We performed a convergence study under increasing levels of mesh refinement for the triaxial verification simulations with the material properties given in Table 2. The maximum imposed axial strain rate 1.5% is discretized into 25 load increments, resulting in a time-step of 0.6 minutes and incremental axial strain of 0.06%. We do not consider convergence with respect to time-step refinement and take the time-step as a constant. The error analysis consists of calculating the difference between the numerically derived axial effective stress at the end of the simulation and analytical solutions:

$$\text{error} = \sqrt{\frac{\int_\Omega \left(\sigma'_a - \sigma'_{a,\text{ann}}\right)^2 \mathrm{d}\Omega}{\int_\Omega \left(\sigma'_{a,\text{ann}}\right)^2 \mathrm{d}\Omega}} \tag{21}$$

where σ'_a is the axial effective stress resulting from numerical simulation and $\sigma'_{a,\text{ann}}$ is an analytical solution. Effective stresses in the numerical solution are approximated by piecewise constants of order zero. We consider two simulation cases for error analysis: (1) undrained triaxial test without plasticity to explore the poromechancial coupling and (2) drained triaxial test with plasticity to explore the elastoplastic coupling. The analytical solutions for axial effective stress to the two simulation cases are (compression positive):

$$\sigma'_{a,\text{ann}} = \begin{cases} \frac{1.5\times10^{-2}E}{1-(1-2\nu)\frac{\alpha B}{3}}\left(1-\frac{B}{3}\right) & \text{case 1} \\ \frac{\sigma'_r\left(1\pm^1\frac{2M_\phi}{3}\right)\pm^1 c_\phi}{1\pm^2\frac{M_\phi}{3}} & \text{case 2} \end{cases} \tag{22}$$

$$\text{compression}: \quad \pm^1 = + \quad \pm^2 = -$$

$$\text{extension}: \quad \pm^1 = - \quad \pm^2 = +$$

where E is the Young's modulus, 1.5×10^{-2} is the imposed axial strain, ν is the Poisson's ratio, B is Skempton's pore pressure coefficient, and σ'_r is the effective radial stress. We simulate four mesh refinement levels with mesh element size varying between 2.5 and 10 mm (equal to 0.2 and 0.8 times the modeling domain radius). The three-dimensional unstructured mesh is generated with the open source software Gmsh [Geuzaine and Remacle, 2009].

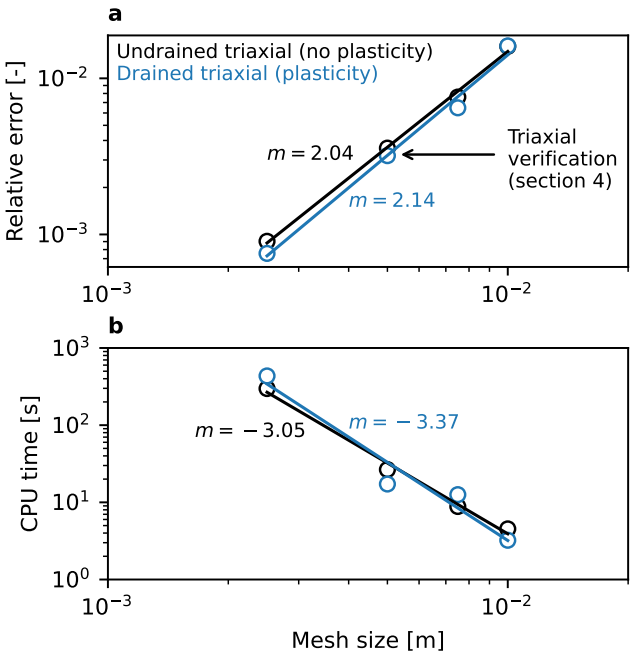

Figure 2. Convergence study with respect to mesh size. **(a)** Error against analytical solutions given by Eqs. 21 and 22. We use a mesh size of 5 mm (1,390 elements) in section 4. **(b)** CPU run time for increasing levels of mesh refinement.

Results show that the numerical solutions reach errors in the range of 10^{-2} to 10^{-3} for the given modeling cases and mesh size, providing confidence in the numerical formulation and solution scheme (Figure 2a). The error is roughly the same for the two modeling cases showing the ability of numerical solutions to accurately model poromechanical and elastoplastic couplings. The simulations exhibit a $O(\Delta h^2)$ convergence, typical for implicit Euler methods. Furthermore, the monolithic solution scheme and selected mesh size results in total CPU time of less than 7.5 minutes with the simulations solved on a single processor (Figure 2b). The CPU time is mostly the same whether plasticity

is active or not because the required number of Newton iterations per time step is the same ($\sim 3-4$). We utilize a mesh element size of 5×10^{-3} - shown graphically on Figure 2a - in the following triaxial simulations to balance CPU run time and solution error. Our chosen mesh size reaches an error of 3×10^{-3} with CPU run time of 3 minutes.

4.2. Displacement Controlled Tests

Under drained triaxial compression, perfectly plastic materials reach a limiting axial stress at yield and remain at that state of stress throughout additional loading. The analytical solution for the limiting axial stress in terms of Drucker-Prager yield criterion is given by case 2 in Eq. 22 and it is equal to 35 MPa, resulting in limiting deviatoric stress of 25 MPa with radial effective stress of 10 MPa (Figure 3a). Volumetric plastic dilation ($\psi > 0$) does not affect the limiting deviatoric stress nor the effective stress path but causes changes in bulk volume during rock yield (Figure 3b). Pore pressure remains constant in the drained test ($k = 10^{-13}\text{m}^2$) despite changes in rock pore volume for $\psi > 0$ and results in a similar deviatoric stress path as the case without dilation (Figure 3c). Notice that the drained deviatoric loading follows a conventional triaxial stress path of $q = 3p'$ while in the elastic region and remains on the yield surface at yield.

The displacement controlled undrained triaxial test can be split into two parts: (1) elastic deformation causing an increase in pore pressure - similar to the theory of one dimensional consolidation [Cheng, 2016] - and (2) plastic dilation during yield causing a decrease in pore pressure and, thus, an increase in radial effective stress. As a result, there is no limiting axial stress as radial effective stress continues to increase with additional deviatoric strain (Figure 4a). For example, the numerical solution predicts an axial stress of > 35 MPa at an axial strain of 1.5 % for a dilation angle of $\psi = 7.5°$ and $k = 10^{-20}\text{m}^2$. Furthermore, pore pressure initially increases during elastic consolidation to $\sim$ 4 MPa but decreases quickly once plastic dilation increase the pore volume (Figure 4b). Note that the pore pressure eventually becomes negative at high enough deviatoric strain, a non-physical event that could be prevented in the real experiment by water cavitation or initial pore pressure larger than the change caused by plastic dilation, but displays the ability of the numerical code to simulate such coupled poroelastic behavior.

The undrained deviatoric stress path can also be split into two parts: (1) elastic deviatoric loading following $q > 3p'$ (different than the drained stress path due to pore pressure coupling and near isochoric response) and (2) increase of both q and p' exactly following the yield surface such that $q = M_\phi p'$ (Figure 4c). Initially, pore pressure increase causes pure deviatoric loading and near constant volume deformation but reverses the trend once the rock yields and dilates. Moreover, the theoretical slope of the elastic stress path (prior to yield) is equal to $q/p' = 3/(1-B)$ with two end-member cases: (1) $q/p' = \infty$ for $K << K_f$ (water saturated soils) and (2) $q/p' = 3$ for $K >> K_f$ (gas saturated rocks and stiff basement rocks). The slope of the elastic stress path in the undrained simulation is $q/p' \approx 11.8$ (Figure 4c), which closely follows the theoretical value of $3/(1-B)$ and provides confidence in the numerical code to simulate undrained response.

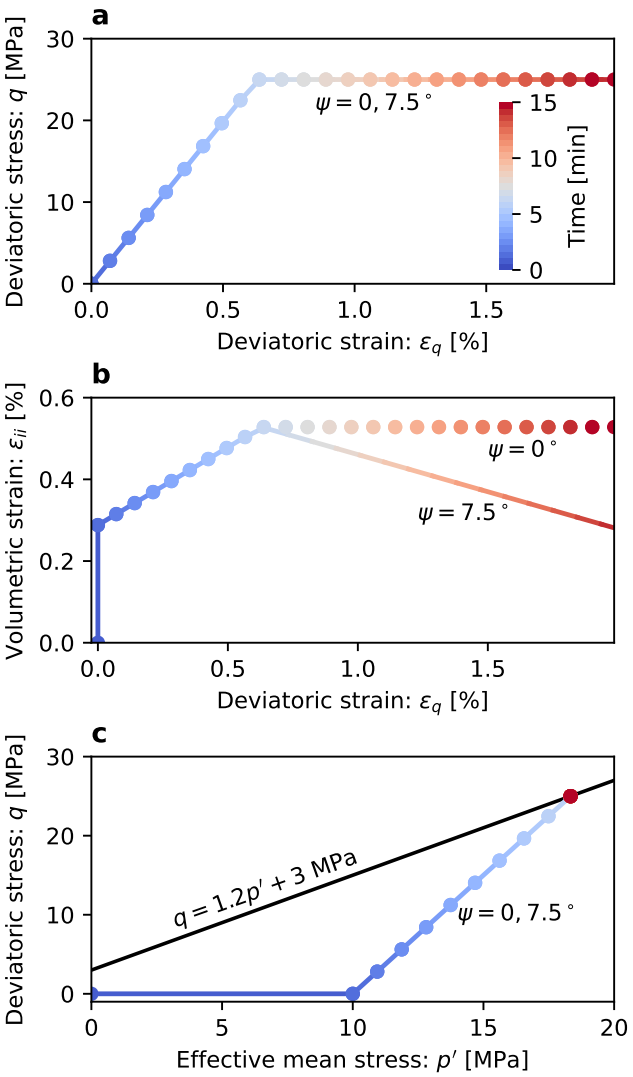

Figure 3. Numerical simulation of a displacement controlled drained triaxial compression test. **(a)** Deviatoric stress vs deviatoric strain for tests with dilation and without dilation (both tests follow same stress path). **(b)** Bulk volume remains unchanged at yield for $\psi = 0°$, yet dilates for $\psi > 0$. **(c)** Stress path in p', q space. Both tests follow the same stress path as pore pressure is unaffected by dilation.

4.3. Temperature Controlled Tests

This subsection verifies the numerical solution against a temperature controlled triaxial test with constant radial total stress of 10 MPa (i.e., confinement), fixed axial displacement, and incrementally applied thermal loads on either flat end of the rock sample (thermal insulation boundary condition in the radial direction). Here, we consider both drained

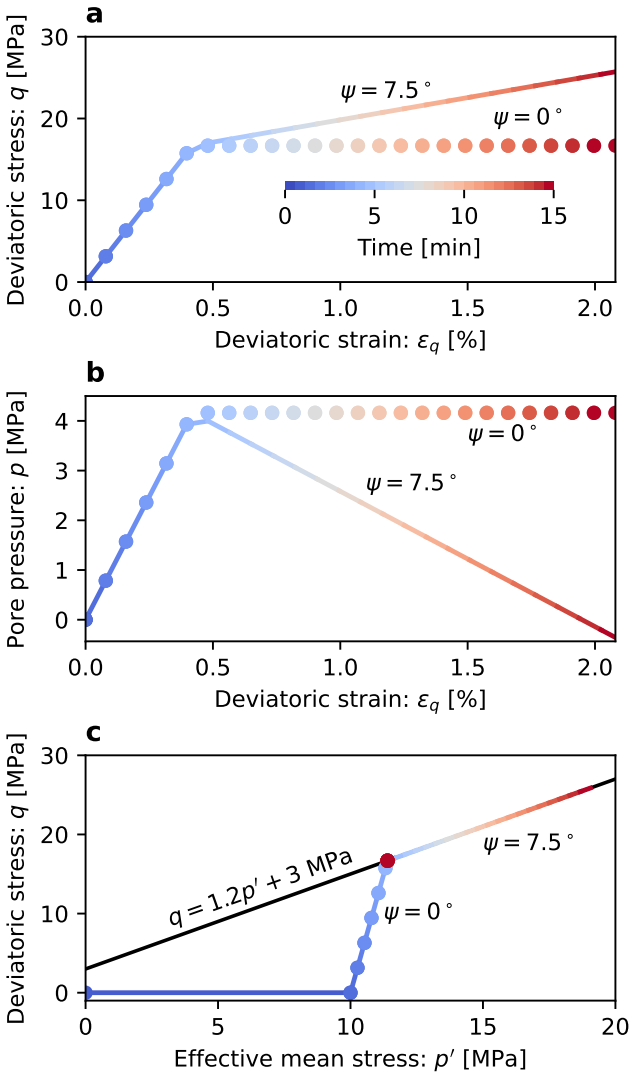

Figure 4. Numerical simulation of a displacement controlled undrained triaxial compression test. **(a, b)** Rock dilation at yield reduces pore pressure (and, thus, effective radial stress increases), making the material stronger because of effective stress-dependent friction. **(c)** Stress path in p', q space for the case with and without dilation.

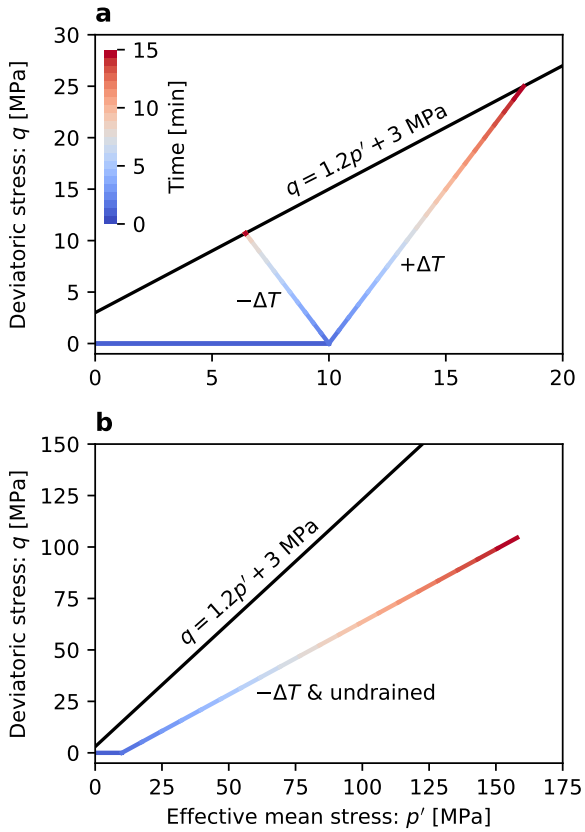

Figure 5. Numerical simulation of a temperature controlled triaxial compression ($+\Delta T$) and extension ($-\Delta T$) test. The confining pressure is constant and the axial displacements at end faces are fixed. **(a)** Drained test with no change in pore pressure and **(b)** undrained test with pore pressure decrease due to contrasting thermal expansion coefficients between solid and fluid.

and undrained tests enforced by changing permeability values (Table 2). The thermal diffusivity is set to 10^{-2} m^2/s, orders of magnitude larger than typical geomaterials, to simulate instantaneous heating/cooling of the entire sample.

Stress paths for the drained temperature controlled test are shown in Figure 5a, with thermal compression test being identical to mechanical compression test (see Figure 5a-compression and Figure 3c). This test is intended to simulate drained thermo-mechanical behavior, in which the influence of different thermal expansion coefficients between solid matrix and pore fluid is inconsequential. While in the elastic regime, thermal loading follows $q = 3p'$ for the case of heating and follows $q = -3p'$ for the case of cooling. As pore pressure remains constant, the analytical limiting deviatoric stress in compression (heating) is $q = 25.0$ MPa and in extension (cooling) is $q = 10.714$ MPa with $\sigma'_r > \sigma'_a$. The numerical solution predicts $q = 24.99$ MPa (heating) and $q = 10.704$ MPa (cooling), a relative error of 4×10^{-4} and 9×10^{-4}, respectively (Figure 5a). The error is computed in a similar way as Eq. 21 but with a volume averaged deviatoric stress, i.e., $q = \frac{1}{V}\int_\Omega q \mathrm{d}\Omega$.

The undrained temperature controlled test is intended to highlight the implications of different thermal expansion coefficients between fluid and the solid matrix on effective stress. This situation arises in cooling of enhanced geothermal systems reservoirs, e.g., [Salimzadeh et al., 2018], and in undrained caprock response to geologic carbon storage reservoirs where injection of CO_2 cools the reservoir within and around the plume, e.g., [Thompson et al., 2021]. The undrained thermo-poroelastic stress path is shown in Figure 5b. Notice that the state of stress remains in the elastic regime despite lowering the temperature by 250 °C. This occurs due to significant decrease in pore pressure as the expected behavior is: $\Delta p = M\beta_e \Delta T$ [Cheng, 2016]. As a result, the stress path follows $q = 0.7p'$ which is not enough

to intersect the shear yield line ($0.7 < M_\phi$). This simulation verifies that the numerical solution is able to simulate full thermo-poroelastic coupling including undrained response to cooling.

5. Example Full-scale Simulations

This section provides example simulations of (1) a closed-loop geothermal system with multiple horizontal wellbores that impose partially undrained thermal cooling and (2) a compartmentalized high-permeability reservoir subject to fluid injection that mostly exhibits drained response. Both simulations are modeled in three-dimensions with local mesh refinement near the wellbores (mesh size of 10 m for the closed-loop wellbore and mesh size of 4 m for the compartmentalized reservoir). Total degrees of freedom are 4.02×10^6 for the closed-loop model and 1.39×10^6 for the compartmentalized reservoir model. The full-scale simulations are intended to (1) provide an application of the numerical code at field scale and (2) compare the numerical results to analytical results for further verification. The simulations were not subject to a mesh convergence study as numerical results compare well to expected theoretical results. In subsection 5.1, we present results for 30-year heat drainage from a basement rock with low permeability (near undrained response) and in subsection 5.2 we present results for 6-months of a constant rate injector with small temperature difference between injection fluid and reservoir.

5.1. Closed-loop geothermal wellbores

5.1.1. Numerical Model Setup

Closed-loop geothermal systems are primarily used for direct use applications such as heating and cooling with more than 84% of geothermal heat pumps utilizing a closed-loop system in the US [Geothermal Technologies Office, 2019]. However, recent interest has focused on deep reservoirs with the potential for electrical power production, e.g., [Beckers et al., 2022, Yuan et al., 2023]. Deep closed-loop systems do not require reservoir stimulation nor permeable fracture networks, and hence avoid early thermal breakthrough caused by thermal short-circuiting [Gee et al., 2021, McLean and Espinoza, 2023]. Rather, low temperature working fluids circulate within a closed wellbore or multiple wellbores, with no exchange between rock pore fluid and working fluid, and extract heat from the surrounding rock [Livescu et al., 2023].

Here, we simulate a closed-loop geothermal system composed of 5 horizontal wellbores that are 1 km in length and spaced 100 m apart, similar to planned projects [Eavor, 2022] (Figure 6). Initial conditions are: (1) geothermal gradient of 30 °C/km, (2) hydrostatic pore pressure, (3) total vertical stress gradient of 23 MPa/km, (4) total maximum horizontal stress gradient of 19 MPa/km, and (5) total minimum horizontal stress gradient of 16 MPa/km. Normal faulting stress regime near critically stressed conditions are most favorable for yield driven by lateral thermal destressing [McLean and Espinoza, 2023]. The basement rock reservoir is located at a depth of 5 km with properties listed in Table 3. The compressive strength and deformation modulus values assumes a large-scale volume average rather than the rock matrix strength, e.g., included effect of a sparse preexisting fracture distribution on overall rock mass strength. Total vertical stress at a depth of 5 km is applied on the top of the model, tectonic displacements are prescribed on north and east boundaries, and roller condition is prescribed everywhere else to obtain the initial state of stress. Other boundary conditions consist of constant hydrostatic pore pressure and thermal insulation along the outer boundaries and no flow along the top and base. The lateral wellbore temperature distribution follows analytical solutions given by Ramey Jr [1962] and will not be repeated here. The temperature distribution is a Dirichlet boundary condition to simulate working fluid extracting heat from the reservoir initially at 175 °C at the depth of wellbores. Discretization details for the wellbores are provided in Appendix B.

Table 3. Poro-elastoplastic properties for deep closed-loop geothermal simulation.

Property	Value	Unit
Bulk modulus: K	37	GPa
Shear modulus: G	21	GPa
Biot modulus: M	94	GPa
Biot coefficient: α	0.56	-
Uniaxial comp. strength: UCS	69.0	MPa
Friction angle: ϕ	30	°
Dilation angle: ψ	7.5	°
Permeability: k	10^{-20}	m^2
Porosity: n	0.009	-
Solid expansion: β_d	6×10^{-5}	1/°C
Fluid mass expansion: β_e	3.5×10^{-5}	1/°C
Thermal diffusivity: α_T	1.4×10^{-6}	m^2/s

5.1.2. Results

Results show that the numerical solution predicts temperature, pore pressure, and stress changes due to cooling - without fluid exchange with wellbores -, as expected for the given reservoir properties and boundary conditions (Figure 7). Temperature decreases everywhere along the length of the wellbores by 100 °C and by ~ 30 °C between wellbores after 30-years, mostly limited by small rock thermal diffusivity. Temperature remains unchanged far away from wellbores throughout the simulation. Continuous geothermal reservoir cooling over several decades cases pore pressure to decrease by 2.5 MPa due to (1) contrasting thermal expansion coefficients between rock matrix and pore fluid and (2) low rock permeability. This is illustrated in the second column of Figure 7, which is also comparable to the undrained temperature controlled triaxial verification test (Figure 5b). This response is not fully undrained as the required permeability for thermal-hydraulic undrained response is on the order of 10^{-23} m^2 [Salimzadeh et al., 2018].

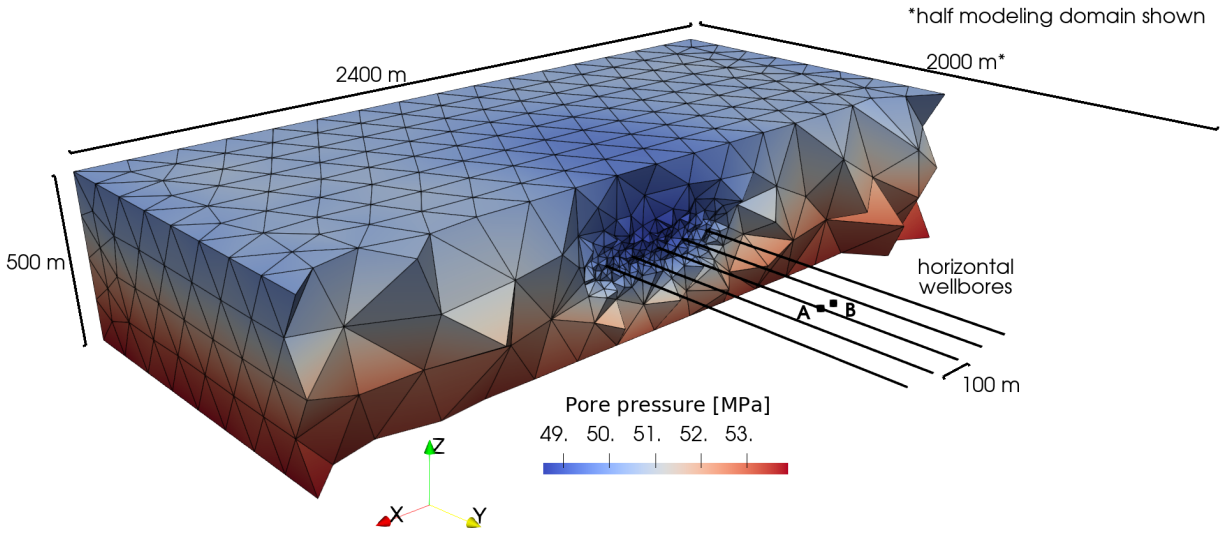

Figure 6. Closed-loop geothermal system with five horizontal wells: numerical modeling domain and mesh. The image shows the pore pressure field with partially undrained response to cooling at the end of the simulation. Points A and B are shown here for stress path analysis - Point A is adjacent to the wellbore and Point B is between wellbores.

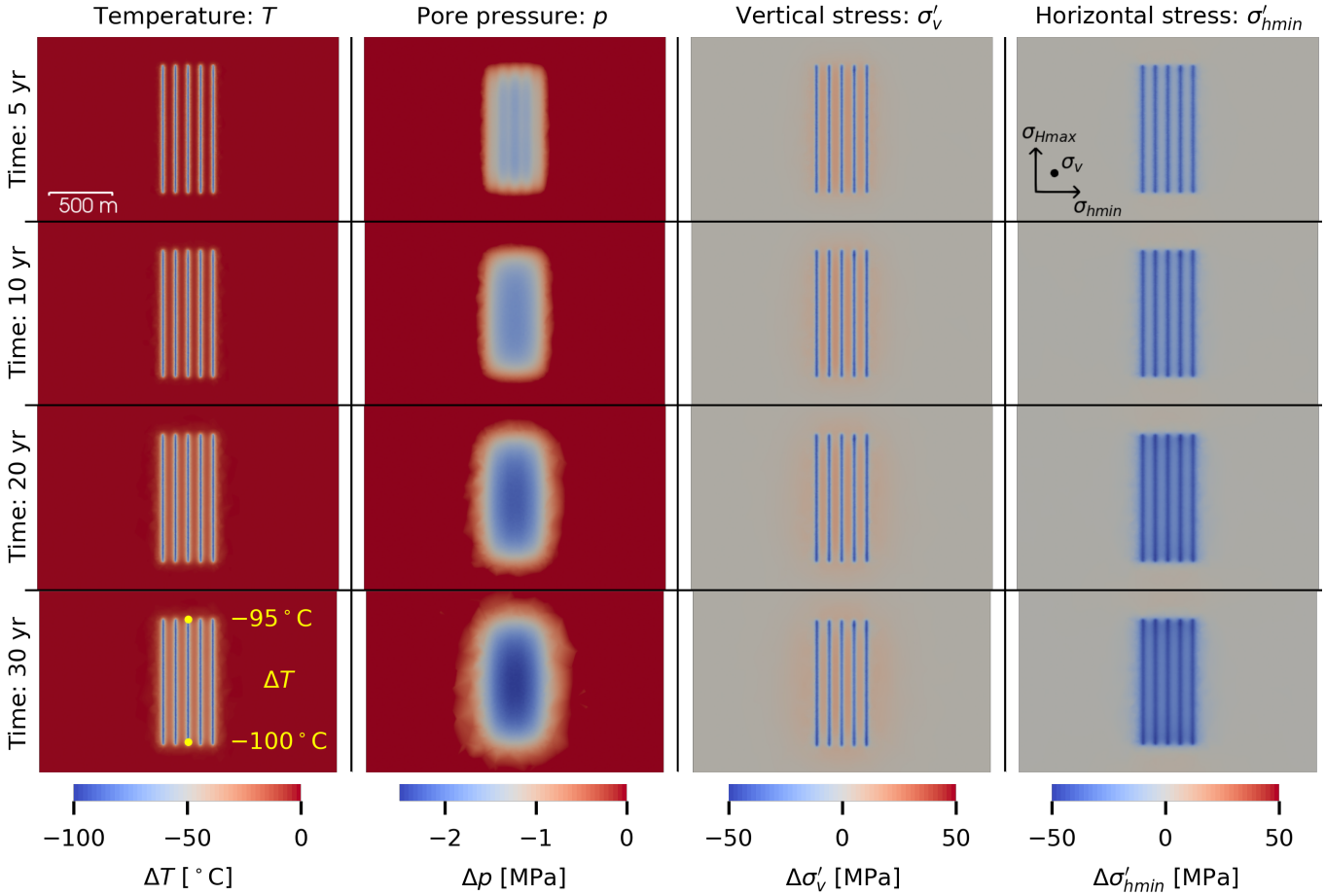

Figure 7. Temperature, pore pressure, and effective stress changes for 30-year heat drainage (horizontal cross-section passing through the depth of the wellbores). Here, changes $\Delta(\cdot)$ refer to the current value with respect to initial conditions. Cooling of the geothermal reservoir leads to (1) partially undrained response, (2) redistribution of total vertical stress around wellbores, and (3) horizontal effective stress relaxation.

The mechanical response of a deep closed-loop geothermal system is complex because (1) the partially undrained behavior alters effective stress throughout the 30-year simulation, (2) thermal unloading causes total vertical stress

to increase between wellbores - an effect of stress redistribution similar to arching in tunnels - and (3) rock shear failure limits the decrease of horizontal effective stresses. Initial cooling everywhere along the length of the wellbore causes total vertical stress to decrease within the cooled volume, but redistribution of overburden stress concentrates between wellbores, increasing deviatoric stress. As thermal drawdown propagates further away from the wellbores, the induced compressive vertical stress decreases but always stays in compression. For example, vertical effective stress initially increases 30 MPa in compression but tends to ~ 5 MPa in compression after several years of heat drainage. Furthermore, horizontal effective stresses decrease everywhere near the wellbores as a result of laterally constrained rock contraction. However, the decrease of horizontal effective stresses is limited by rock yield in regions that reach shear failure.

Although temperature does not change far away from the wellbores, effective stresses and pore pressure do (Figure 8). Above and below the cooled rock volume, horizontal effective stresses increases 5 MPa in compression - also a result of compressive stress redistribution around the wellbores. Hence, normal faults are more likely to reactivate within the cooled rock volume but reverse faults are more likely to reactivate outside of the cooled volume as predicted by analytical solutions [Segall and Fitzgerald, 1998]. These results in Figure 8 illustrate the ability of the numerical solution to solve and predict coupled fields that operate under different spatial extents and time scales, e.g., temperature only decreases close to the wellbores yet induces deformation and pressure changes far away.

Lastly, the numerical solution shows that reservoir cooling in critically stressed deep closed-loop geothermal systems can drive the state of stress to shear failure (Figure 9). Although more complex than the simple triaxial verification tests, the stress path to reach shear failure follows expectations for the given stress and pore pressure changes. Locations adjacent to the wellbores (point A on Figure 9a) yield within 10 years of heat drainage while locations between wellbores (point B on Figure 9a) stay in the elastic regime for more than 30-years because the initial state of stress favors shear failure by nearly isotropic unloading. The stress path adjacent to the wells initially follows a deviatoric loading path as (1) horizontal effective stresses decrease much more than vertical effective stress and (2) pore pressure decreases, keeping mean stress nearly constant. However, the stress path changes in later times and follows an isotropic unloading path where all three principal effective stresses decrease simultaneously. By the end of 30-year heat drainage, the volume of rock within ~ 30 m of the wellbores is near yield conditions (Figure 9b). This illustrates that the elastoplastic model (specifically the closed-form solution to the elastoplastic return map - Eq. 10) can accurately simulate rock yield under combined thermal, hydraulic, and mechanical loading.

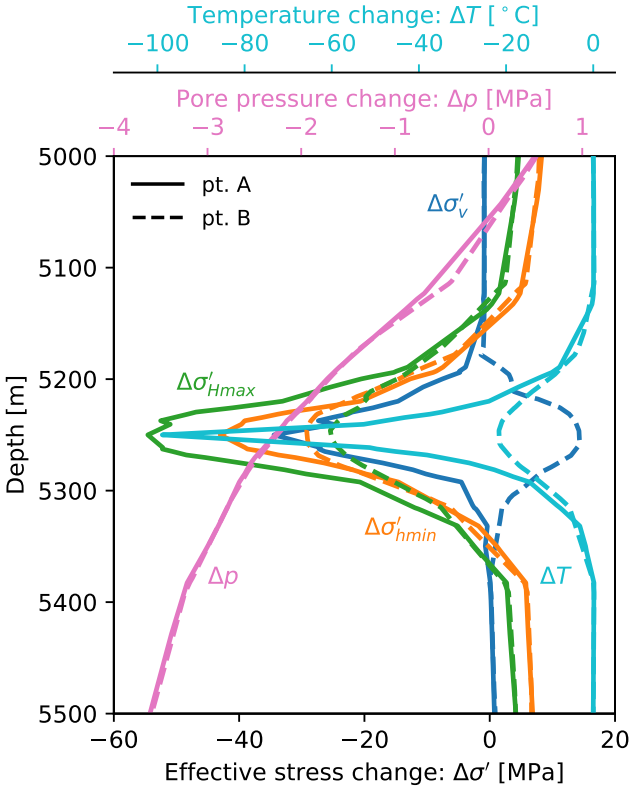

Figure 8. Effective stress and pore pressure profiles after 30-years of heat drainage. Solid and dashed lines indicate a vertical profile passing through point A and point B, respectively.

5.2. Fluid Injection in Compartmentalized Reservoir

5.2.1. Numerical Model Setup

This section provides an example numerical simulation of a compartmentalized reservoir subject to non-isothermal fluid injection, e.g., enhanced oil recovery with water flooding, salt-water disposal, and CO_2 geological storage. For simplicity, we neglect multiphase fluid flow and multiphase poroelasticity in the formulation but could be added with (1) additional equations for phase mass balance and (2) updated constitutive equations for fluid compressibility, Biot modulus, Cauchy stress, capillary pressure, etc. [Lewis and Schrefler, 1998]. We simulate a constant rate injector well for 6-months in a 50 m thick high-permeability reservoir that is bounded by 50 m thick low permeability caprock and baserock (Figure 10). Initial conditions are: (1) geothermal gradient of 30 °C/km, (2) hydrostatic pore pressure, and (3) total vertical stress gradient of 23 MPa/km together with total (isotropic) horizontal stress gradient of 15.5 MPa/km.

The injector is perforated the entire 50 m height of the reservoir, which is at 2 km depth. Total vertical stress at a depth of 2 km is applied on the top of the model, tectonic displacements are prescribed on north and east boundaries, and roller condition is prescribed everywhere else to obtain the initial state of stress. Non-isothermal injection is applied through the Dirac delta function, restricting the

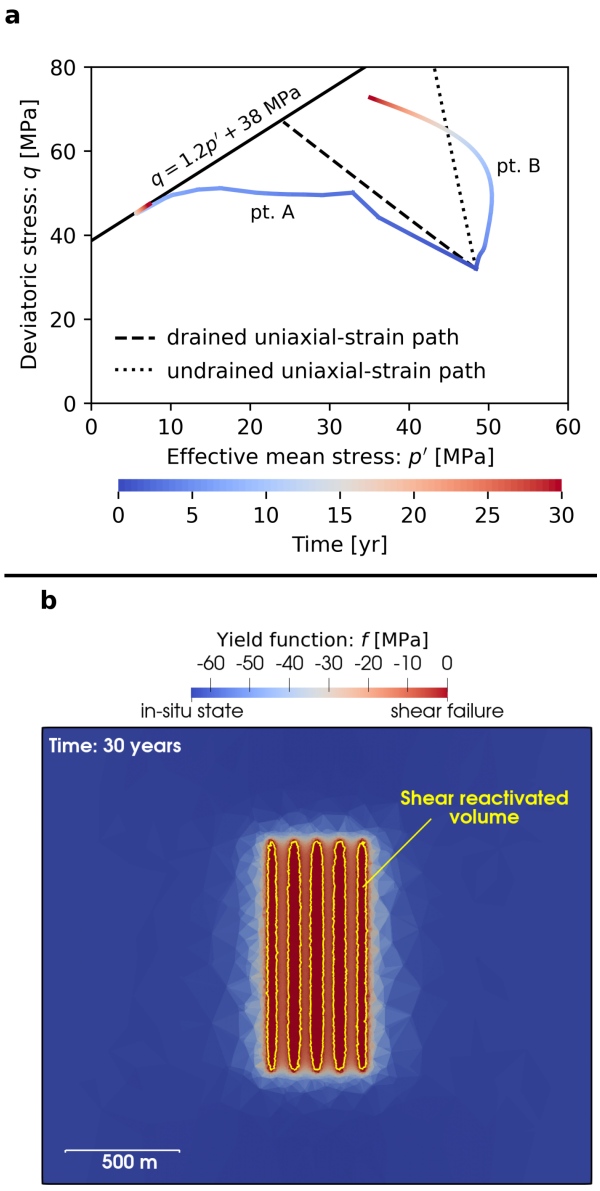

Figure 9. **(a)** Stress paths through 30-years of heat drainage. Locations adjacent to the wellbores (point A) reach shear failure where thermal unloading is most pronounced but locations between wellbores (point B) stay in the elastic region for more than 30-years. **(b)** Shear reactivated reservoir volume shown for a horizontal cross-section at the depth of the lateral wellbores.

source term to the degrees of freedom associated with the interior well nodes (refer to f^p and f^T in Eqs. 18 and 20). A total volume of 28,617 m^3 is injected at a temperature of 50 °C over the 6-month simulation in the compartmentalized reservoir - injection rate of 1,000 bbl per day - (Figure 10). The large injection rate was chosen such that (1) pore pressure increases enough to cause yield everywhere in the reservoir and (2) thermal advection is significantly larger than thermal diffusion. Hence, this model verifies the streamline upwind Petrov-Galerkin method for heat transport. Reservoir and caprock properties are shown in Table 4 with the same elastic constants for both layers. Note that the high Poisson's ratio has two effects: (1) results in initially large horizontal effective stress -without tectonic stresses- due to $\sigma'_h = \frac{\nu}{1-\nu}\sigma'_v$ and (2) ensures injection induced stress changes cause rock yield everywhere in the reservoir within the 6-month injection period, i.e., $\nu = 0.3$ is a choice informed by the analytical solution (Eq. 22) to maximize isotropic component of the stress path such that $|\Delta q/\Delta p'| \leqslant M_\phi$, causing yield with sufficient pore pressure increase.

Table 4. Poro-elastoplastic properties for fluid injection simulation.

Property	Value	Unit
Bulk modulus: K	8.3	GPa
Shear modulus: G	3.8	GPa
Biot modulus: M	9.2	GPa
Biot coefficient: α	0.78	-
Uniaxial comp. strength: UCS	5.0	MPa
Friction angle: ϕ	30	°
Dilation angle: ψ	7.5	°
Permeability: k	1×10^{-14}, 5×10^{-19}	m^2
Porosity: n	0.02	-
Solid expansion β_d:	3×10^{-5}	1/°C
Fluid mass expansion β_e:	5.7×10^{-5}	1/°C
Thermal diffusivity α_T:	7.5×10^{-7}	m^2/s

5.2.2. Results

The results show that the numerical solution can accurately simulate rock yield driven by pore pressure increase alone and by pore pressure increase combined with temperature decrease. Locations near the injector (within the thermal front) reach shear failure quickly because the mechanical response is intensified by temperature contrast between injection fluid and reservoir (Figure 11a). This occurs within 25 m of the injector by the end of the injection period. Assuming total vertical stress remains constant, the 1D-strain analytical solution for a poroelastic stress path due to pore pressure increase is:

$$\Delta q = \left(\frac{1}{2\eta} - \frac{2}{3}\right)^{-1} \Delta p' \approx 0.63\Delta p' \tag{23}$$

where $\eta = \alpha(1-2\nu)/2(1-\nu) = 0.22$ is the poroelastic stress coefficient [Cheng, 2016]. Any deviation from this solution arises from additional thermal stresses within the cooled region and 3D geometrical effects. As expected, mean effective stress exhibits more pronounced decreases near the injector (point A) and the stress path mostly follows $\Delta q = 0.55\Delta p'$, up to 12.5% away from the analytical solution. After the rock yields near the injector, all three principal effective stresses continue to decrease with continued injection and results in a stress path directly following the yield surface $q = M_\phi p'$ (Figure 11a at time equal to 4 months). Furthermore, locations outside the thermal front (point B) closely follow the analytical stress path of $\Delta q = 0.63\Delta p'$ because temperature decrease near the injector does not change much the total

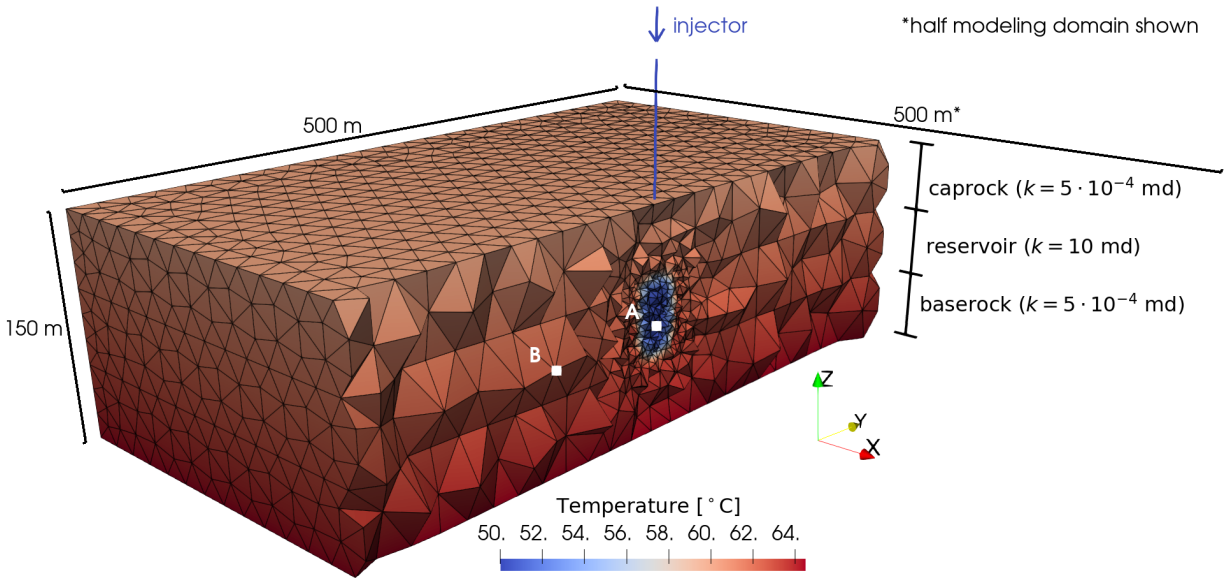

Figure 10. Numerical modeling domain and mesh for fluid injection simulation. Points A and B are shown here for stress path analysis - point A is within the thermal front (thermo-poroelastic response) and point B is ahead of the thermal front (poroelastic response).

vertical stress far away (Figure 11b). These locations further away from the injector stay in the elastic region for about 1.3 times as long as those locations within the thermal front, e.g., 5.5 months compared to 4.25 months.

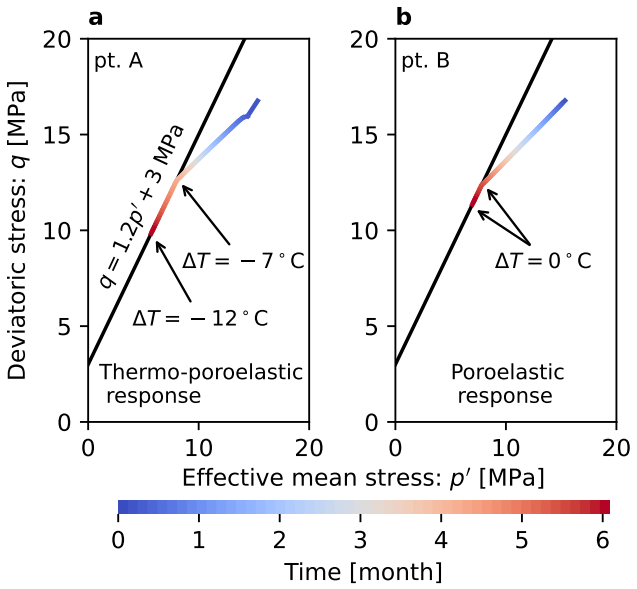

Figure 11. Stress paths for compartmentalized reservoir subject to fluid injection. **(a)** Effective stress changes are larger within the thermal front and reach shear failure quickly. **(b)** Shear failure is delayed outside the thermal front where no temperature change occurs.

The difference in stress changes between locations within and ahead of the thermal front is large, particularly for vertical effective stress (Figure 12). Total vertical stress remains nearly constant far away from the injector but decreases considerably within the thermal front, similar to vertical stress redistribution around cooled wellbores in section 5.1. Yet, the difference in horizontal effective stress change between points A and B is smaller because rock cooling near the injector causes forced contraction everywhere in the reservoir (a result of adjacent rock causing a virtual lateral constraint). Furthermore, rock shear failure limits the decrease in all effective stresses which otherwise would go far beyond the yield surface - even to tension - if elastoplasticity was not included. Our results are in agreement with those of [Im et al., 2021] which conclude that assuming a purely elastic reservoir subject to non-isothermal fluid injection can result in unreasonable results because calculated tensile stress may become much larger than the tensile strength of rocks and the state of stress may go far beyond the shear yield surface.

6. Conclusion

The numerical modeling and understanding of coupled THM processes in complex 3D domains is of increasing importance in a wide range of subsurface activities. Preset open source codes and commercial codes limit the end user's ability to change many aspects of the software package and some are limited to purely elastic reservoir response. Most existing codes do not formulate mechanically induced porosity changes based on the theory of thermo-poroelastoplasticity, neglecting possible undrained response to reservoir cooling. This work provides a freely available and end user adaptable thermo-poroelastoplastic numerical code and solutions for subsurface applications. The objectives of the numerical model are to: (1) incorporate stress, pressure, and porosity constitutive behavior based on the theory of thermo-poroelasticity, (2) extend traditional

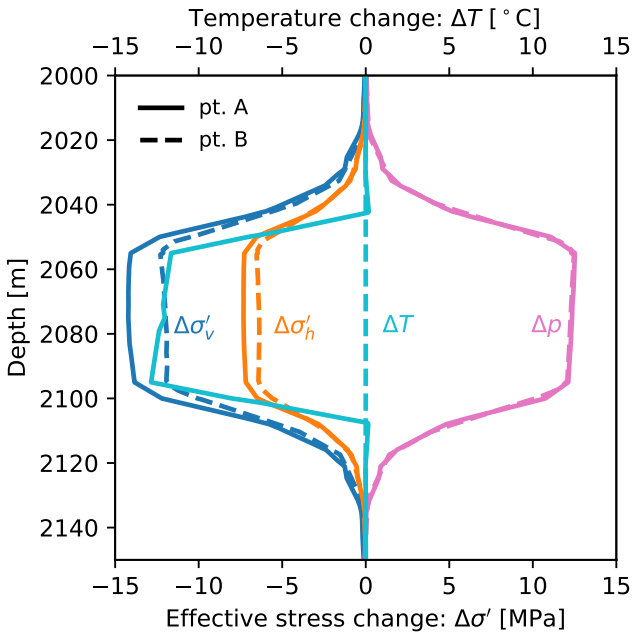

Figure 12. Effective stress and pore pressure profiles after 6-months of fluid injection. Solid and dashed lines indicate a vertical profile passing through the thermal front and outside the thermal front, respectively. Differences between solid and dashed lines represent thermal stresses. The difference in pressure for points A and B is negligible as permeability is large and pressure changes propagate quickly.

THM elastic coupling to include effects of rock mass inelasticity, (3) utilize a locally mass conserving finite element discretization for mass balance, (4) preserve numerical stability in the presence of advection dominated energy transport, and (5) utilize open source computing platforms such that paid licensing barriers are prevented. The numerical solution was formulated in the variational form and verified against several conventional triaxial tests with three-dimensional simulations compared against analytical solutions. We provided two reservoir scale example simulations of (1) a deep closed-loop geothermal reservoir and (2) a compartmentalized reservoir subject to non-isothermal fluid injection. Our results show that the numerical solution accurately predicts coupled temperature, pore pressure, and stress changes for the given reservoir properties and boundary conditions. Lastly, the results show that accurate prediction of THM coupled processes in the subsurface may need to include plastic strains because assuming a purely elastic response may yield unreasonable results for large stress changes.

Conflicts of Interest

The authors declare that they have no known competing financial interests or personal relationships that could have appeared to influence the work reported in this article .The complete review history is available online.

Acknowledgements

This work was supported by the Hildebrand Initiatives program at the Hildebrand Department of Petroleum and Geosystems Engineering at The University of Texas at Austin. Freely available software used in this work include: Fenicsx (`https://fenicsproject.org/`), ParaView (`https://www.paraview.org/`), Gmsh (`https://gmsh.info/`), Overleaf LaTex platform (`https://www.overleaf.com/`), and Anaconda (`https://www.anaconda.com/`).

Data Availability

The numerical code has been made freely available at the following GitHub repository: `https://github.com/Matt-L-McLean/poromechanics`

Appendix A. Strain Softening Model

Elastic-perfectly plastic models are unable to capture changes of rock strength after the onset of yield. However, it is well known that rocks usually experience a decrease in shear strength at the onset of yield unless confining pressure is sufficiently large to cause continuous yield over large deviatoric strains with no decrease in shear strength [Franklin, 1971, Schwartz, 1964]. Moreover, reactivation of preexisting fractures distributed within a rock mass may smooth the asperities at the fracture face and, hence, reduce the bulk shear strength of the rock mass [Patton, 1966]. Shear strength degradation from peak to residual values - after the onset of yield - has been documented in small scale laboratory tests and observed in large scale field applications of rock masses [Hoek and Brown, 1997, Read and Hegemier, 1984]. In this section, we formulate and provide example simulations of a strain softening material that more accurately describes the constitutive behavior of either (1) intact rocks at low confining pressure or (2) rock masses with preexisting planes of weakness - without explicitly modeling those planes of weakness. This method is preferable over modeling discrete fracture plasticity (refer to Garipov and Hui [2019]) for densely fractured media that may be impractical to mesh and model with contact mechanics. Furthermore, this method is a simple extension from the perfectly plastic model in section 2.3, utilizing a similar yield function and plastic potential but with variation in the size of the yield surface.

A.1. Changes to the Elastoplastic Model

Three changes are required to extend the perfectly plastic model to strain softening behavior: inclusion of (1) mobilized friction angle η^*, (2) mobilized plastic dilatancy, and (3) softening modulus H in the plastic multiplier to increase plastic strain magnitude. The mobilized friction parameter η^* - takes the place of M_ϕ in section 2.3 - is assumed to be a nonlinear function of accumulated plastic shear strain $\varepsilon_q^p = \left(\frac{2}{3}\left(\mathrm{dev}\left(\varepsilon^p\right)_{ij}\mathrm{dev}\left(\varepsilon^p\right)_{ij}\right)\right)^{1/2}$ and bounded between a peak η_p^* and residual η_r^* value [Potts et al., 2001]:

$$\eta^* = \eta_p^* - \left(\eta_p^* - \eta_r^*\right)\left[1 - \exp\left(-a\varepsilon_q^p\right)\right] \tag{24}$$

where a is a parameter that controls how quickly rock strength decreases, e.g., $a = \infty$ corresponds to brittle failure while $a = 0$ is perfectly plastic. The exponential model is chosen for ease of numerical implementation over a linear model that takes the form of a piecewise function with possible discontinuous derivatives. We assume that cohesive strength remains constant, but it may also vary with accumulated plastic shear strain. Moreover, the dilation angle - M_ψ in section 2.3 - is replaced with a mobilized dilation angle (equal to $\eta^* - \eta_r^*$) which provides dilation while yielding and constant volume deformation once the residual strength has been reached (similar to critical state plastic dilatancy). Lastly, the plastic multiplier $\mathrm{d}\lambda$ includes a softening modulus H and is equal to:

$$\mathrm{d}\lambda = \frac{\langle f\left(\sigma'^{,e}_{ij}\right)\rangle_+}{3G + K\left(\eta^* - \eta_r^*\right)\eta^* + H} \tag{25}$$

with $H = -\frac{\partial f}{\partial \eta^*}\frac{\mathrm{d}\eta^*}{\mathrm{d}\varepsilon_q^p}\frac{\partial g}{\partial q} = -p' a\left(\eta_p^* - \eta_r^*\right)\exp\left(-a\varepsilon_q^p\right) < 0$ for decreasing rock strength. The closed form solution to the plastic multiplier results from the analytical derivative $\frac{\mathrm{d}\eta^*}{\mathrm{d}\varepsilon_q^p}$. Note that H decreases to zero for sufficiently large values of plastic shear strain and the strength weakening model reduces to an elastic-perfectly plastic model without plastic dilation, i.e., $\eta^* = \eta_r^*$ and $H = 0$.

A.2. Undrained Triaxial Simulation

We simulate a displacement controlled undrained triaxial test with the properties given in Table 2, $\eta_p^* = 1.2$ (friction coefficient of 0.577), $\eta_r^* = 1.0$ (friction coefficient of 0.467), and the weakening parameter $a = 100$. The total imposed axial strain is 5% such that large amounts of plastic shear strain are accumulated and the mobilized friction parameter can decrease close to the residual value. The axial loading rate is 0.1% per minute and time-step is 36 seconds, the same as in section 4, which results in a total simulation time of 50 minutes. The load rate is consistent with section 4 to ensure undrained response, i.e., characteristic pore pressure diffusion time much less than the time-step.

The simulation results show that the numerical simulation predicts stress and pore pressure changes as expected for the given boundary conditions and constitutive law (Figure 13). The mobilized friction parameter controls the size of the yield surface and decreases non-linearly with increasing deviatoric strain (Figure 13a). Pore pressure increases during elastic compression to ~ 4 MPa then decreases with additional axial displacement. Pore pressure decrease after yield approaches a constant value (~ 0 MPa) as the mobilized dilation angle (equal to $\eta^* - \eta_r^*$) becomes zero and, hence, reaches critical state (Figure 13b). Volumetric strain takes a similar trend to pore pressure but it is not shown here. Lastly, the undrained effective stress path with shear strength degradation is shown on Figure 13c. The stress path after the onset of yield is bounded by the peak and residual shear strength lines, as expected. Our simulation results are in agreement with analytical solutions of strain softening undrained stress paths from Wood [2004].

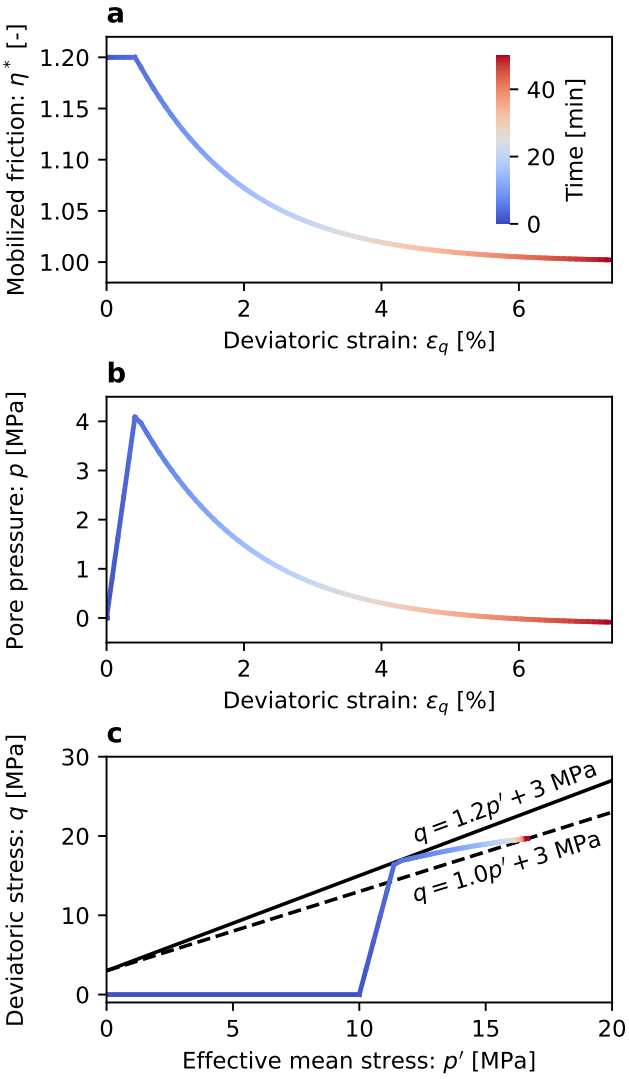

Figure 13. Numerical simulation of an undrained triaxial compression with strain softening behavior. **(a)** The mobilized friction parameter decreases from peak to residual value. **(b)** Dilation at yield reduces pore pressure but approaches constant volume deformation with $\eta^* \approx \eta_r^*$. **(c)** Effective stress path in p', q space.

Appendix B. Discretization of Lateral Wellbores

Poromechanical simulation of a deep closed-loop geothermal system requires discretization of the lateral wellbores. Explicitly modeling the wellbore as a cylinder that is taken out of the modeling domain is impractical to mesh for field scale simulations as the aspect ratio between wellbore radius and reservoir length can be $> 10^4$ and may cause (1) issues in mesh creation and (2) large increase in total degrees of freedom. This approach is similar to that of modeling a circular cavity in a rock mass with stress amplification at the cavity wall, e.g., wellbore stability analysis. We, therefore, model the wellbore with a one-dimensional line embedded in a three-dimensional reservoir with the temperature

degrees of freedom (linear shape function) coinciding with the line (Figure 14). Stress amplification in the near wellbore region does not occur with this method. We utilize a 10 m cell diameter mesh size for those elements adjacent to the interior line. The wellbore temperature - lower than the surrounding rock temperature - is a Dirichlet boundary condition imposed on the line. Note that we are mainly interested in the long-term poromechanical reservoir response to heat drainage rather than accurately predicting fluid outlet temperature from a closed-loop geothermal system. Hence, we do not model wellbore mass balance nor energy balance but utilize analytical solutions for wellbore temperature that varies in time and along the lateral length, e.g., Ramey Jr [1962].

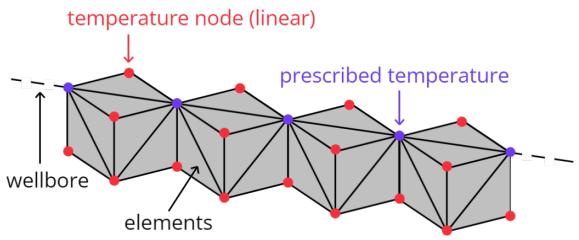

Figure 14. Spatial discretization of the later wellbores in a deep closed-loop geothermal system.

References

Allis, R., Moore, J., Davatzes, N., Gwynn, M., Hardwick, C., Kirby, S., McLennan, J., Pankow, K., Potter, S., and Simmons, S. (2016). Egs concept testing and development at the milford, utah forge site. In *41st Workshop on Geothermal Reservoir Engineering*. Stanford University.

Bai, M. and Abousleiman, Y. (1997). Thermoporoelastic coupling with application to consolidation. *International Journal for Numerical and analytical methods in Geomechanics*, 21(2):121–132.

Balay, S., Abhyankar, S., Adams, M. F., Benson, S., Brown, J., Brune, P., Buschelman, K., Constantinescu, E. M., Dalcin, L., Dener, A., Eijkhout, V., Faibussowitsch, J., Gropp, W. D., Hapla, V., Isaac, T., Jolivet, P., Karpeev, D., Kaushik, D., Knepley, M. G., Kong, F., Kruger, S., May, D. A., McInnes, L. C., Mills, R. T., Mitchell, L., Munson, T., Roman, J. E., Rupp, K., Sanan, P., Sarich, J., Smith, B. F., Zampini, S., Zhang, H., Zhang, H., and Zhang, J. (2022). PETSc Web page. `https://petsc.org/`.

Beckers, K. F., Rangel-Jurado, N., Chandrasekar, H., Hawkins, A. J., Fulton, P. M., and Tester, J. W. (2022). Techno-economic performance of closed-loop geothermal systems for heat production and electricity generation. *Geothermics*, 100.

Ben-Zion, Y. and Sammis, C. G. (2013). Shear heating during distributed fracturing and pulverization of rocks. *Geology*, 41(2):139–142.

Berger, L., Bordas, R., Kay, D., and Tavener, S. (2017). A stabilized finite element method for finite-strain three-field poroelasticity. *Computational Mechanics*, 60:51–68.

Biot, M. A. (1941). General theory of three-dimensional consolidation. *Journal of Applied Physics*, 12(2):155–164.

Brezzi, F., Douglas, J., and Marini, L. D. (1985). Two families of mixed finite elements for second order elliptic problems. *Numerische Mathematik*, 47(2):217–235.

Brooks, A. N. and Hughes, T. J. (1982). Streamline upwind/petrov-galerkin formulations for convection dominated flows with particular emphasis on the incompressible navier-stokes equations. *Computer methods in applied mechanics and engineering*, 32(1-3):199–259.

Cheng, A. H.-D. (2016). *Poroelasticity*, volume 27. Springer.

Coussy, O. (2004). *Poromechanics*. John Wiley & Sons.

Drucker, D. C. and Prager, W. (1952). Soil mechanics and plastic analysis or limit design. *Quarterly of Applied Mathematics*, 10(2):157–165.

Eavor (2022). Eavor-lite. `https://www.eavor.com/eavor-lite/`.

Evans, K. F., Cornet, F. H., Hashida, T., Hayashi, K., Ito, T., Matsuki, K., and Wallroth, T. (1999). Stress and rock mechanics issues of relevance to HDR/HWR engineered geothermal systems: review of developments during the past 15 years. *Geothermics*, 28(4-5):455–474.

Fang, Y., Nguyen, B. N., Carroll, K., Xu, Z., Yabusaki, S. B., Scheibe, T. D., and Bonneville, A. (2013). Development of a coupled thermo-hydro-mechanical model in discontinuous media for carbon sequestration. *International Journal of Rock Mechanics and Mining Sciences*, 62:138–147.

Franceschini, A., Castelletto, N., and Ferronato, M. (2021). Approximate inverse-based block preconditioners in poroelasticity. *Computational Geosciences*, 25(2):701–714.

Franklin, J. A. (1971). Triaxial strength of rock materials. *Rock Mechanics Felsmechanik Mecanique des Roches*, 3(2):86–98.

Frigo, M., Castelletto, N., Ferronato, M., and White, J. A. (2021). Efficient solvers for hybridized three-field mixed finite element coupled poromechanics. *Computers & Mathematics with Applications*, 91:36–52.

Garipov, T. and Hui, M. (2019). Discrete fracture modeling approach for simulating coupled thermo-hydro-mechanical effects in fractured reservoirs. *International Journal of Rock Mechanics and Mining Sciences*, 122.

Gee, B., Gracie, R., and Dusseault, M. B. (2021). Multi-scale short-circuiting mechanisms in multiple fracture enhanced geothermal systems. *Geothermics*, 94.

Geothermal Technologies Office (2019). Geovision: Harnessing the heat beneath our feet. Technical report, United States Department of Energy.

Geuzaine, C. and Remacle, J.-F. (2009). Gmsh: A 3-d finite element mesh generator with built-in pre-and post-processing facilities. *International journal for numerical methods in engineering*, 79(11):1309–1331.

Ghassemi, A. (2012). A review of some rock mechanics issues in geothermal reservoir development. *Geotechnical and Geological Engineering*, 30(3):647–664.

Gueguen, Y. and Bouteca, M. (1999). Mechanical properties of rocks: pore pressure and scale effects. *Oil & Gas Science and Technology*, 54(6):703–714.

Haagenson, R., Rajaram, H., and Allen, J. (2020). A generalized poroelastic model using fenics with insights into the

noordbergum effect. *Computers & Geosciences*, 135.

Habera, M. and Zilian, A. (2022). dolfiny. `https://github.com/michalhabera/dolfiny`.

Hoek, E. and Brown, E. T. (1997). Practical estimates of rock mass strength. *International journal of rock mechanics and mining sciences*, 34(8):1165–1186.

Im, K., Avouac, J.-P., Heimisson, E. R., and Elsworth, D. (2021). Ridgecrest aftershocks at coso suppressed by thermal destressing. *Nature*, 595(7865):70–74.

Itasca Consulting Group, Inc. (2019). *FLAC3D – Fast Lagrangian Analysis of Continua in Three-Dimensions, Ver. 7.0*. Itasca.

Jung, H., Espinoza, D. N., and Hosseini, S. A. (2020). Wellbore injectivity response to step-rate CO2 injection: Coupled thermo-poro-elastic analysis in a vertically heterogeneous formation. *International Journal of Greenhouse Gas Control*, 102.

Kelkar, S., Lewis, K., Karra, S., Zyvoloski, G., Rapaka, S., Viswanathan, H., Mishra, P., Chu, S., Coblentz, D., and Pawar, R. (2014). A simulator for modeling coupled thermo-hydro-mechanical processes in subsurface geological media. *International Journal of Rock Mechanics and Mining Sciences*, 70:569–580.

Kim, J. (2010). *Sequential methods for coupled geomechanics and multiphase flow*. Stanford University.

Kivi, I. R., Pujades, E., Rutqvist, J., and Vilarrasa, V. (2022). Cooling-induced reactivation of distant faults during long-term geothermal energy production in hot sedimentary aquifers. *Scientific Reports*, 12(1).

Kohl, T., Evansi, K., Hopkirk, R., and Rybach, L. (1995). Coupled hydraulic, thermal and mechanical considerations for the simulation of hot dry rock reservoirs. *Geothermics*, 24(3):345–359.

Kolditz, O., Bauer, S., Bilke, L., Böttcher, N., Delfs, J.-O., Fischer, T., Görke, U. J., Kalbacher, T., Kosakowski, G., McDermott, C., et al. (2012). Opengeosys: an open-source initiative for numerical simulation of thermo-hydro-mechanical/chemical (thm/c) processes in porous media. *Environmental Earth Sciences*, 67(2):589–599.

Lewis, R. W. and Schrefler, B. A. (1998). *The finite element method in the static and dynamic deformation and consolidation of porous media*. John Wiley.

Lindsay, A. D., Gaston, D. R., Permann, C. J., Miller, J. M., Andrš, D., Slaughter, A. E., Kong, F., Hansel, J., Carlsen, R. W., Icenhour, C., et al. (2022). 2.0-moose: Enabling massively parallel multiphysics simulation. *SoftwareX*, 20.

Livescu, S., Dindoruk, B., Schulz, R., Boul, P., Kim, J., and Wu, K. (2023). Geothermal and electricity production: Scalable geothermal concepts in the future of geothermal in texas: Contemporary prospects and perspectives. *UT Faculty/Researcher Works*.

Logg, A., Mardal, K.-A., and Wells, G. (2012). *Automated solution of differential equations by the finite element method: The FEniCS book*, volume 84. Springer Science & Business Media.

Logg, A. and Wells, G. N. (2010). Dolfin: Automated finite element computing. *ACM Transactions on Mathematical Software (TOMS)*, 37(2):1–28.

Martínez-Garzón, P., Kwiatek, G., Sone, H., Bohnhoff, M., Dresen, G., and Hartline, C. (2014). Spatiotemporal changes, faulting regimes, and source parameters of induced seismicity: A case study from the geysers geothermal field. *Journal of Geophysical Research: Solid Earth*, 119(11):8378–8396.

McLean, M. L. and Espinoza, D. N. (2023). Thermal destressing: Implications for short-circuiting in enhanced geothermal systems. *Renewable Energy*, 202:736–755.

McTigue, D. F. (1986). Thermoelastic response of fluid-saturated porous rock. *Journal of Geophysical Research*, 91(B9).

Mortensen, J. J. (1978). Hot dry rock: a new geothermal energy source. *Energy*, 3(5):639–644.

National Research Council et al. (1996). *The Waste Isolation Pilot Plant: A Potential Solution for the Disposal of Transuranic Waste*. National Academies Press.

Nemeth, K. J. (2004). Southeast regional carbon sequestration partnership (secarb). Technical report, Southern States Energy Board (US).

Olivella, S., Gens, A., Carrera, J., and Alonso, E. (1996). Numerical formulation for a simulator (code_bright) for the coupled analysis of saline media. *Engineering computations*, 13(7):87–112.

Palciauskas, V. V. and Domenico, P. A. (1982). Characterization of drained and undrained response of thermally loaded repository rocks. *Water Resources Research*, 18(2):281–290.

Pan, H. and Rui, H. (2012). Mixed element method for two-dimensional darcy-forchheimer model. *Journal of Scientific Computing*, 52:563–587.

Pandey, S., Vishal, V., and Chaudhuri, A. (2018). Geothermal reservoir modeling in a coupled thermo-hydro-mechanical-chemical approach: A review. *Earth-Science Reviews*, 185:1157–1169.

Patton, F. D. (1966). *Multiple modes of shear failure in rock and related materials*. University of Illinois at Urbana-Champaign.

Phillips, P. J. and Wheeler, M. F. (2007a). A coupling of mixed and continuous galerkin finite element methods for poroelasticity i: the continuous in time case. *Computational Geosciences*, 11(2).

Phillips, P. J. and Wheeler, M. F. (2007b). A coupling of mixed and continuous galerkin finite element methods for poroelasticity ii: the discrete-in-time case. *Computational Geosciences*, 11(2):145–158.

Phillips, P. J. and Wheeler, M. F. (2008). Overcoming the problem of locking in linear elasticity and poroelasticity: an heuristic approach. *Computational Geosciences*, 13(1):5–12.

Potts, D. M., Zdravković, L., Addenbrooke, T. I., Higgins, K. G., and Kovačević, N. (2001). *Finite element analysis in geotechnical engineering: application*, volume 2. Thomas Telford London.

Ramey Jr, H. J. (1962). Wellbore heat transmission. *Journal of petroleum Technology*, 14(04):427–435.

Read, H. E. and Hegemier, G. A. (1984). Strain softening of rock, soil and concrete–a review article. *Mechanics of materials*, 3(4):271–294.

Rutqvist, J. (2011). Status of the tough-flac simulator and recent applications related to coupled fluid flow and crustal deformations. *Computers & Geosciences*, 37(6):739–750.

Rutqvist, J. (2012). The geomechanics of co2 storage in deep sedimentary formations. *Geotechnical and Geological Engineering*, 30(3):525–551.

Salimzadeh, S., Nick, H. M., and Zimmerman, R. (2018). Thermoporoelastic effects during heat extraction from low-permeability reservoirs. *Energy*, 142:546–558.

Schwartz, A. E. (1964). Failure of rock in the triaxial shear test. In *The 6th US Symposium on Rock Mechanics (USRMS)*. OnePetro.

Segall, P. and Fitzgerald, S. D. (1998). A note on induced stress changes in hydrocarbon and geothermal reservoirs. *Tectonophysics*, 289(1-3):117–128.

Streit, J. E. and Hillis, R. R. (2004). Estimating fault stability and sustainable fluid pressures for underground storage of co2 in porous rock. *Energy*, 29(9-10):1445–1456.

Thompson, N., Andrews, J. S., and Bjørnarå, T. I. (2021). Assessing potential thermo-mechanical impacts on caprock due to co2 injection–a case study from northern lights ccs. *Energies*, 14(16).

Ugueto, G. A., Wojtaszek, M., Huckabee, P. T., Savitski, A. A., Guzik, A., Jin, G., Chavarria, J. A., and Haustveit, K. (2021). An integrated view of hydraulic induced fracture geometry in hydraulic fracture test site 2. In *9th Unconventional Resources Technology Conference*. American Association of Petroleum Geologists.

Wilkins, A., Green, C. P., and Ennis-King, J. (2021). An open-source multiphysics simulation code for coupled problems in porous media. *Computers & Geosciences*, 154.

Wood, D. M. (2004). *Geotechnical modelling*. Taylor & Francis.

Xia, Y., Podgorney, R., and Huang, H. (2017). Assessment of a hybrid continuous/discontinuous galerkin finite element code for geothermal reservoir simulations. *Rock Mechanics and Rock Engineering*, 50(3):719–732.

Yuan, W., Chen, Z., Grasby, S. E., Little, E., and Zhao, G. (2023). Thermodynamic modeling of the advanced geothermal system using inclined well applications. *Applied Thermal Engineering*, 220.

Manuscript received 10th February 2023, revised 30th August 2023, accepted 2nd October 2023.